# Origin of oxidized mercury in the summertime free troposphere over the southeastern US

V. Shah[1], L. Jaeglé[1], L. E. Gratz[2], J.L. Ambrose[3,a], D. A. Jaffe[1,3], N. E. Selin[4],
S. Song[4], T. L. Campos[5], F. M. Flocke[5], M. Reeves[5], D. Stechman[5], M. Stell[5],
J. Festa[6], J. Stutz[6], A. J. Weinheimer[7], D. J. Knapp[7], D. D. Montzka[7],
G. S. Tyndall[7], E. C. Apel[7], R. S. Hornbrook[7], A. J. Hills[7], D. D. Riemer[8],
N. J. Blake[9], C. A. Cantrell[10], and R. L. Mauldin III[10,11]

[1]Department of Atmospheric Sciences, University of Washington, Seattle, WA, USA
[2]Environmental Program, Colorado College, Colorado Springs, CO, USA
[3]School of Science, Technology, Engineering and Mathematics,
University of Washington-Bothell, Bothell, WA, USA
[4]Department of Earth, Atmospheric and Planetary Sciences, Massachusetts Institute of Technology,
Cambridge, MA, USA
[5]Earth Observing Laboratory, National Center for Atmospheric Research, Boulder, CO, USA
[6]Department of Atmospheric and Oceanic Sciences, University of California, Los Angeles,
Los Angeles, CA, USA
[7]Atmospheric Chemistry Observations and Modeling Laboratory, National Center for Atmospheric
Research, Boulder, CO, USA
[8]Rosenstiel School of Marine and Atmospheric Science, University of Miami, Miami, FL, USA
[9]Department of Chemistry, University of California, Irvine, Irvine, CA, USA
[10]Department of Atmospheric and Oceanic Sciences, University of Colorado, Boulder, CO, USA
[11]Department of Physics, University of Helsinki, Helsinki, Finland
[a]now at: College of Engineering and Physical Sciences, University of New Hampshire, Durham,
NH, USA

*Correspondence to:* V. Shah (vshah@uw.edu)

**Abstract.** We collected mercury observations as part of the Nitrogen, Oxidants, Mercury, and Aerosol Distributions, Sources, and Sinks (NOMADSS) aircraft campaign over the southeastern US between 1 June and 15 July 2013. We use the GEOS-Chem chemical transport model to interpret these observations and place new constraints on bromine radical initiated mercury oxidation chem-

5   istry in the free troposphere. We find that the model reproduces the observed mean concentration of total atmospheric mercury (THg) (observations: $1.49 \pm 0.16 \, \mathrm{ng \, m^{-3}}$, model: $1.51 \pm 0.08 \, \mathrm{ng \, m^{-3}}$), as well as the vertical profile of THg. The majority (65 %) of observations of oxidized mercury (Hg(II)) ~~are~~ were below the instrument's detection limit (detection limit per flight: 58–228 $\mathrm{pg \, m^{-3}}$), consistent with model-calculated Hg(II) concentrations of 0–196 $\mathrm{pg \, m^{-3}}$. However, for observa-

10  tions above the detection limit we find that modeled Hg(II) concentrations are a factor of 3 too low (observations: $212 \pm 112 \, \mathrm{pg \, m^{-3}}$, model: $67 \pm 44 \, \mathrm{pg \, m^{-3}}$). The highest Hg(II) concentrations, 300–680 $\mathrm{pg \, m^{-3}}$, were observed in dry (RH < 35 %) and clean air masses during two flights over Texas at 5–7 km altitude and off the North Carolina coast at 1–3 km. The GEOS-Chem model, back tra-

jectories and observed chemical tracers for these air masses indicate subsidence and transport from

15  the upper and middle troposphere of the subtropical anticyclones, where fast oxidation of elemental

mercury (Hg(0)) to Hg(II) and lack of Hg(II) removal lead to efficient accumulation of Hg(II). We

hypothesize that the most likely explanation for the model bias is a systematic underestimate of the

$Hg(0) + Br$ reaction rate. We find that sensitivity simulations with tripled bromine radical concentra-

tions or a faster oxidation rate constant for $Hg(0) + Br$, result in 1.5–2 times higher modeled Hg(II)

20  concentrations and improved agreement with the observations. The modeled tropospheric lifetime of

Hg(0) against oxidation to Hg(II) decreases from 5 months in the base simulation to 2.8–1.2 months

in our sensitivity simulations. In order to maintain the modeled global burden of THg, we need to

increase the in-cloud reduction of Hg(II), thus leading to faster chemical cycling between Hg(0) and

Hg(II). Observations and model results for the NOMADSS campaign suggest that the subtropical

25  anticyclones are significant global sources of Hg(II).


## 1   Introduction

Exposure to mercury affects the human nervous system, hinders cognitive development in children,

and causes cardiovascular diseases in adults (Mergler et al., 2007; Karagas et al., 2012). In fish, mam-

mals, and birds, mercury can adversely affect reproductive behavior (Scheuhammer et al., 2007).

30  Although mercury is naturally present in our environment, human activities have increased its con-

centrations in the atmosphere and ocean by factors of 3 to 7 (Lamborg et al., 2002; Selin, 2009;

Strode et al., 2010; Amos et al., 2013; Zhang et al., 2014) making mercury exposure a major public

health concern.

In the troposphere, 90 % of mercury occurs in its elemental form (Hg(0)) in the gas phase, while

35  the rest is in the oxidized (mercuric, +2) state (Hg(II)), either in the gas-phase or bound to particles

(Gustin et al., 2013). The chemical forms of atmospheric Hg(II) have not been identified, but labo-

ratory and theoretical studies suggest that they likely include $HgCl_2$, $HgBr_2$, $HgBrBrO$, $HgBrNO_2$,

$HgBrHO_2$, $HgO$, $HgSO_4$, $Hg(NO_3)_2$, and $Hg(OH)_2$ (Gustin et al., 2013; Dibble et al., 2012; Huang

et al., 2015). Both natural and anthropogenic processes emit mercury to the atmosphere, mostly as

40  Hg(0). Atmospheric Hg(II) originates predominantly from the oxidation of Hg(0), with a minor con-

tribution from direct anthropogenic emissions (Driscoll et al., 2013). Unlike Hg(0), Hg(II) is highly

water-soluble and reactive, and is quickly scavenged from the atmosphere by rainwater or aerosol

particles, such that 60 % of the global mercury deposition is estimated to occur by wet and dry

deposition of Hg(II) (Selin et al., 2008; Holmes et al., 2010).

45  Atomic bromine (Br) has been observed as the main oxidant of atmospheric Hg(0) in the polar

and the marine boundary layers (Lindberg et al., 2002; Ebinghaus et al., 2002; Laurier et al., 2003;

Obrist et al., 2011), and laboratory studies (Ariya et al., 2002; Donohoue et al., 2006), theoretical

calculations (Goodsite et al., 2004, 2012; Balabanov et al., 2005; Dibble et al., 2012; Shepler et al.,

2

2007), and modeling studies (Holmes et al., 2006, 2010) suggest a predominant role of Br in the oxidation of Hg(0) in the global atmosphere. While other oxidants have been proposed, in particular OH and $O_3$ (Hall, 1995; Spicer et al., 2002; Pal and Ariya, 2004a, b; Sumner et al., 2005; Rutter et al., 2012), theoretical studies (Calvert and Lindberg, 2005; Goodsite et al., 2004; Hynes et al., 2009) suggest that the bimolecular reaction of Hg(0) with $O_3$ and OH is too slow in the atmosphere, and the fast rates observed in the laboratory could have been influenced by wall-mediated reactions or formation of aerosol particles (Tossell, 2006; Subir et al., 2011).

Measurements at a few high-elevation sites have shown episodic enhancements of Hg(II) concentrations (350–600 $pg\,m^{-3}$) usually in low relative humidity and low CO air, suggesting efficient in situ production of Hg(II) in the free troposphere (Landis et al., 2005; Swartzendruber et al., 2006; Fain et al., 2009; Sheu et al., 2010; Weiss-Penzias et al., 2015). Sillman et al. (2007) reported higher (60–248 $pg\,m^{-3}$) Hg(II) concentrations at 3 km altitude than near the surface in aircraft flights off the Florida coast. Swartzendruber et al. (2009) found a large variability in Hg(II) concentrations (0–500 $pg\,m^{-3}$) during five flights over the Pacific Northwest below 5 km altitude, with higher concentrations in free-tropospheric air with low aerosol concentrations. Lyman and Jaffe (2012), found enhanced Hg(II) concentrations of $\sim 450\,pg\,m^{-3}$ and depleted total mercury (THg, THg = Hg(0) + Hg(II)) concentrations ($< 1\,ng\,m^{-3}$) in a stratospheric intrusion, suggesting rapid oxidation of Hg(0) and loss of Hg(II) above the tropopause. During multiple year-round flights over Tennessee, USA, Brooks et al. (2014) found that Hg(II) concentrations at 2–4 km altitude were 10–30 times higher than those near the surface throughout the year. Typically, these past aircraft campaigns have focused on Hg(II) measurements over small spatial scales. The sparseness of free-tropospheric measurements of Hg(II) has hindered the validation of redox chemistry in global models of tropospheric mercury, which display large inter-model variability in wet and dry deposition (Bullock et al., 2008, 2009; Travnikov et al., 2010).

The Nitrogen, Oxidants, Mercury and Aerosol Distributions, Sources, and Sinks (NOMADSS) aircraft campaign was conducted over the southeastern US to determine the distribution of THg and Hg(II) at a regional scale. Here, we analyze these observations using the GEOS-Chem chemical transport model with the goals of examining the origin of Hg(II) in the free troposphere and testing the kinetics of the Br-initiated oxidation mechanism.

## 2   Observations and model used in this study

### 2.1   The NOMADSS campaign

The NOMADSS aircraft campaign was conducted over the southeastern US from 1 June to 15 July 2013 using the NSF/NCAR C-130 aircraft. We conducted 19 research flights of 4–7 h duration each out of Smyrna, Tennessee (36°1′ N, 86°31′ W) (Fig. 1). NOMADSS was part of the larger Southeast Atmosphere Study (SAS), a collaborative effort to characterize the atmospheric composition

3

over the southeastern US (http://www.eol.ucar.edu/field_projects/sas). One of the objectives of the NOMADSS campaign, and the focus of this study, was to quantify the tropospheric distribution of mercury species. Mercury measurements were made using the University of Washington's Detector of Oxidized Mercury Species (UW-DOHGS), which is currently the only instrument capable of making simultaneous measurements of total and elemental mercury concentrations aboard an aircraft platform at a relatively high time resolution of 2.5 min (Swartzendruber et al., 2009; Lyman and Jaffe, 2012; Ambrose et al., 2013, 2015). In addition, the C-130 aircraft was equipped with other instruments summarized in Table 1.

This paper complements several other papers focused on the analysis of mercury measurements during NOMADSS. In particular, Gratz et al. (2015a) present an analysis of the high Hg(II) concentrations and BrO concentrations observed on one NOMADSS flight (research flight 6). Ambrose et al. (2015) use the NOMADSS observations to calculate enhancement ratios of Hg in the plumes of six coal-fired power plants, and compare them to the Hg emission ratios reported in the emission inventories. Song et al. (2014) combine the NOMADSS observations with results from the GEOS-Chem model to constrain Hg emissions from land and ocean sources. Gratz et al. (2015b) use the NOMADSS observations over Lake Michigan and a plume dispersion model to quantify the outflow of Hg from the Chicago/Gary industrial area.

### 2.2 The UW-DOHGS instrument

The UW-DOHGS is a dual channel instrument that simultaneously measures concentrations of THg and Hg(0). Ambrose et al. (2015) discuss the configuration of the instrument during NOMADSS, in-flight calibration as well as pre- and post-campaign laboratory tests. Briefly, the UW-DOHGS draws a fast flow of ambient air from a rear-facing aircraft inlet heated to 110 °C to facilitate transmission of Hg(II) compounds. Two Tekran® 2537B Hg vapor analyzers subsample the inlet flow at 1 L min$^{-1}$ (at 0 °C and 1 atm) through parallel channels. The Tekran® analyzers sample Hg(0) by Au-amalgamation pre-concentration on paired sample cartridges, with quantification by cold vapor atomic fluorescence spectrometry (CVAFS). The sample integration time and measurement time resolution are both 2.5 min. In the THg channel, Hg(II) compounds are reduced to Hg(0) by passing the sampled air through a quartz pyrolyzer heated to 650 °C. In the Hg(0) channel, Hg(II) (in gas and particle-bound phases) is removed using either a quartz wool trap (first fourteen flights) or a cation exchange membrane (remaining five flights). Hg(II) concentrations are calculated from the difference between the THg and Hg(0) measurements. ~~The~~ In comparison, the Tekran® 2537-1130-1135 speciation system uses KCl denuders to capture gas-phase oxidized mercury, which is subsequently thermally desorbed as elemental mercury for analysis (Landis et al., 2002). The measurement cycle of the Tekran® speciation system is 30 minutes or longer, compared to the 2.5 minute cycle for the UW-DOHGS. The UW-DOHGS is not affected by O$_3$-interference, unlike the Tekran® ~~2537-1130-1135 speciation system that uses KCl denuders for Hg(II) capture~~ system (Ly-

4

man et al., 2010; Ambrose et al., 2013; McClure et al., 2014). A limitation of UW-DOHGS is that the quartz wool traps can release Hg(II) in humid conditions (Ambrose et al., 2013, 2015), which decreased the number of Hg(II) observations in the boundary layer during the first fourteen flights. This was not a problem on the later five flights when cation exchange membranes were used in place of quartz wool.

During NOMADSS, the $1\sigma$ uncertainty in THg and Hg(0) was 8–10 %, and the detection limit (DL) was $< 0.05\,\mathrm{ng\,m^{-3}}$. For Hg(II), the $1\sigma$ uncertainty varied between $38\,\mathrm{pg\,m^{-3}}$ (at THg of $1.2\,\mathrm{ng\,m^{-3}}$) and $55\,\mathrm{pg\,m^{-3}}$ (at THg of $2.8\,\mathrm{ng\,m^{-3}}$). The Hg(II) DL is calculated using the "same air" configuration, in which the Hg(II) filter is bypassed and both analyzers sample the same air downstream of the pyrolyzer in the THg channel (Ambrose et al., 2013, 2015). The $3\sigma$ Hg(II) DL for the campaign ranged between 58 and $228\,\mathrm{pg\,m^{-3}}$.

The UW-DOHGS instrument was operational during all 19 flights of the NOMADSS campaign, and concentrations of THg were measured continuously during each flight, except during calibration cycles. A total of 2381 (2.5 min average) observations of THg were made during the campaign (Table 23). Hg(II) concentrations could be determined for only $\sim 60$ % of the time (1503 observations), because of periodic in-flight calibration cycles and because of reduced retention efficiency of the Hg(II) traps during some flight segments in the moist boundary layer. For the entire NOMADSS campaign, 35 % of the Hg(II) measurements (528 points out 1503) were above the instrument's DL. Here and in the rest of the paper, we use ADL (Above Detection Limit) observations to refer to Hg(II) measurements above the instrument's DL and BDL (Below Detection Limit) for Hg(II) measurements below the DL. In the boundary layer (defined here as altitude $< 2\,\mathrm{km}$ and water vapor $> 8\,\mathrm{g\,kg^{-1}}$), 87 % of the 532 observations were BDL. In the free troposphere, 53 % out of the 971 observations were BDL.

As more than half the Hg(II) observations during NOMADSS were BDL, we follow the recommendation of Helsel (2011) and use the robust regression on order statistics (ROS) method to assign values for BDL observations. The ROS method assumes a lognormal distribution for the observations, and estimates the distribution's parameters using ADL measurements. The BDL values are then estimated using the fitted distribution. The ROS method is applied to calculate Hg(II) means and standard deviations reported in Tables 1 and 2 and Figs. 2–5.

### 2.3 The GEOS-Chem model

#### 2.3.1 General description

The GEOS-Chem global 3-D atmospheric chemical transport model (www.geos-chem.org) is driven by meteorological fields from the NASA Global Modeling and Assimilation Office (GMAO) Goddard Earth Observing System (GEOS) Version 5 Forward Processing (FP). The GEOS-5 FP system consists of a general circulation model (GCM) coupled with a data assimilation (DAS) system (Rie-

necker et al., 2008), with a native horizontal resolution of 0.25° latitude by 0.3125° longitude and 72 vertical levels up to 0.01 hPa. The GEOS-5 FP meteorological fields are archived either at 1 or 3 h intervals, depending on the variables.

GEOS-Chem includes advection (Lin and Rood, 1996), convective transport (Wu et al., 2007), turbulent mixing (Lin and McElroy, 2010), wet deposition (Liu et al., 2001; Wang et al., 2011; Amos et al., 2012), and dry deposition (Wang et al., 1998; Zhang et al., 2011) of chemical species. The full-chemistry simulation includes an up-to-date chemical mechanism for gas-phase and heterogeneous reactions of $HO_x$-$NO_x$-VOC-$O_3$-aerosols in the troposphere (Bey et al., 2001) with the recent addition of bromine chemistry (Parrella et al., 2012). We use here GEOS-Chem model version 9-02.

The GEOS-Chem Hg model simulates the emissions, chemistry, transport, and deposition of Hg(0) and Hg(II) in the atmosphere (Selin et al., 2007) with updates from Holmes et al. (2010); Amos et al. (2012), and Zhang et al., 2012), coupled with a 2-D ocean (Strode et al., 2007; Soerensen et al., 2010) and a 2-D land (Selin et al., 2008; Holmes et al., 2010). The model includes prescribed emissions from biomass burning and geogenic activity (Holmes et al., 2010). The global GEOS-Chem Hg simulation, with a resolution of 4° latitude × 5° longitude, was evaluated by Holmes et al. (2010), who found the modeled THg ($1.71 \pm 0.5\,\mathrm{ng\,m^{-3}}$) to be in good agreement with observations ($1.86 \pm 1.0\,\mathrm{ng\,m^{-3}}$, correlation coefficient $= 0.9$) at 39 land-based sites across the globe. Simulated THg concentrations were about $10\,\%$ higher than THg concentrations measured during three aircraft campaigns (INTEX-B, CARIBIC, and ARCTAS), but modeled vertical profiles were consistent with observations in the troposphere. Zhang et al. (2012) developed a nested-grid Hg simulation in GEOS-Chem, using a higher horizontal resolution ($0.5° \times 0.667°$) over North America. They found that the average annual modeled wet deposition ($7.2 \pm 3.2\,\mathrm{\mu g\,m^{-2}\,yr^{-1}}$) at 95 Mercury Deposition Network (MDN; http://nadp.sws.uiuc.edu/mdn/) sites was close to the observations ($8.8 \pm 3.6\,\mathrm{\mu g\,m^{-2}\,yr^{-1}}$) and showed a correlation coefficient of 0.78. The modeled annual mean THg concentrations ($1.42 \pm 0.11\,\mathrm{ng\,m^{-3}}$) were unbiased with respect to the observations ($1.46 \pm 0.11\,\mathrm{ng\,m^{-3}}$) at 19 surface-based sites. While the modeled gaseous Hg(II) concentrations at these sites were higher than the observations by a factor of 1.5, the model captured the observed seasonal cycle, with higher concentrations during spring and summer at most sites.
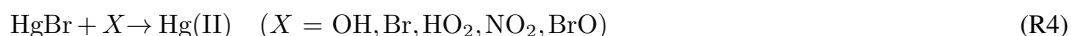
### 2.3.2 Updates to Hg emissions in GEOS-Chem

We have updated the global anthropogenic Hg emissions to the United Nations Environment Programme (UNEP)/Arctic Monitoring and Assessment Program (AMAP) 2010 (http://www.amap.no/mercury-emissions/datasets), and over North America we use the U.S. EPA National Emissions Inventory (NEI) 2011 (http://www.epa.gov/ ttnchie1/net/2011inventory.html) and Environment Canada's National Pollutant Release Inventory (NPRI) 2011 emission inventories. The speciation of anthropogenic emissions is assumed to be $90\,\%$ Hg(0) : $10\,\%$ Hg(II) from all anthropogenic sources based on Zhang et al. (2012) and Kos et al. (2013). For 2013, the GEOS-Chem global emission

of mercury is $1850\,\mathrm{Mg\,a^{-1}}$ from anthropogenic sources, $5025\,\mathrm{Mg\,a^{-1}}$ from natural sources and re-emission, and $225\,\mathrm{Mg\,a^{-1}}$ from biomass burning. For 1 June-15 July 2013, the anthropogenic, natural, and biomass burning emissions over North America are 130, 870 and $22\,\mathrm{d^{-1}}$, respectively.

### 2.3.3 Updates to Hg chemistry in GEOS-Chem

195 The oxidation of Hg(0) is modeled as a two-step reaction initiated by Br radicals as originally implemented in GEOS-Chem by Holmes et al. (2010), based on the work of Goodsite et al. (2004); Donohoue et al. (2006), and Balabanov et al. (2005):

$$\mathrm{Hg(0) + Br \xrightarrow{M} HgBr} \tag{R1}$$

$$\mathrm{HgBr + M \rightarrow Hg(0) + Br + M} \tag{R2}$$

200 $$\mathrm{HgBr + Br \rightarrow Hg(0) + Br_2} \tag{R3}$$

$$\mathrm{HgBr + X \rightarrow Hg(II) \quad (X = OH, Br, HO_2, NO_2, BrO)} \tag{R4}$$

We use the recently corrected rate constant for the HgBr dissociation reaction (R2) (Goodsite et al., 2012). Holmes et al. (2010) had assumed Br and OH as the second-step oxidants (R4). In addition, based on the recommendations of Dibble et al. (2012), we have updated this mechanism to include

205 $\mathrm{HO_2}$, $\mathrm{NO_2}$, and BrO as the second-step oxidants. The rates constants used here are:

$$k_1 = 1.46 \times 10^{-32} \times \left(\frac{T}{298}\right)^{-1.86} \times [\mathrm{M}] \quad \mathrm{cm^{-3}\,molecule^{-1}\,s^{-1}}$$

(Donohoue et al., 2006) \hfill (1)

$$k_2 = 2.67 \times 10^{41} \exp\left(\frac{-7292}{T}\right)\left(\frac{T}{298}\right)^{1.76} \times k_1 \quad \mathrm{s^{-1}} \quad \text{(Goodsite et al., 2012)} \tag{2}$$

$$k_3 = 3.9 \times 10^{-11} \quad \mathrm{cm^{-3}\,molecule^{-1}\,s^{-1}} \quad \text{(Balabanov et al., 2005)} \tag{3}$$

210 $$k_4 = 2.5 \times 10^{-10} \times \left(\frac{T}{298}\right)^{-0.57} \quad \mathrm{cm^{-3}\,molecule^{-1}\,s^{-1}}$$

(Goodsite et al., 2012; Dibble et al., 2012) \hfill (4)

The reduction of Hg(II) to Hg(0) is assumed to occur in cloud droplets in the presence of sunlight. The reduction is assumed to be proportional to the photolysis frequency of $\mathrm{NO_2}$, and the coefficient is estimated by constraining the model results with the observed mean burden of THg in the tro-

215 posphere (Holmes et al., 2010). The uptake of Hg(II) by sea-salt particles is simulated as a kinetic mass transfer process (Holmes et al., 2010). For non sea-salt aerosol particles, gas-particle partitioning is simulated as an equilibrium process based on an empirical relationship (Amos et al., 2012). The modeled wet and dry deposition of gas-phase Hg(II) is analogous to that of $\mathrm{HNO_3}$, and of particle-bound Hg(II) to that of sulfate particles.

### 2.3.4 Simulations conducted for this study

In this study, the GEOS-Chem Hg model is run in a one-way nested-grid configuration, with the native horizontal resolution ($0.25° \times 0.3125°$) over North America, and a coarser resolution ($2° \times 2.5°$) globally. Both, the coarse- and fine-grid models, share the same vertical resolution with 47 layers (13 layers in the bottom $2\,\mathrm{km}$, and 16 layers between 2 and $10\,\mathrm{km}$). The global Hg model is spun-up with a $3\,\mathrm{year}$ simulation, and is then used to generate the initial and boundary conditions for the nested-domain, and to calculate the annual global mercury budget. Monthly concentrations of Br, BrO, OH, $HO_2$, $NO_2$, $O_3$ and aerosols are obtained from a $1\,\mathrm{year}$ $4° \times 5°$ global $HO_x$–$NO_x$–VOC-$O_3$-$BrO_x$-aerosols tropospheric chemistry GEOS-Chem simulation. We run the nested $0.25° \times 0.3125°$ Hg model for North America from 1 June to 15 July 2013. For comparison to the NOMADSS aircraft observations, the model is sampled along the flight track at the $2.5\,\mathrm{min}$ time step of the UW-DOHGS instrument.

In addition to the BASE simulation with the $\mathrm{Hg}(0) + \mathrm{Br}$ chemistry described above (Sect. 2.3.3), we perform ~~two sensitivity simulations~~ five sensitivity simulations (Table 2), and focus on two of them. In the first sensitivity simulation ($3\times$Br) we increase the GEOS-Chem Br and BrO concentrations by a factor of 3 in the $45°\,\mathrm{S}$ to $45°\,\mathrm{N}$ latitude band between $750\,\mathrm{hPa}$ and the tropopause. Parrella et al. (2012) found that the GEOS-Chem BrO is within the BrO measurement uncertainties of the GOME-2 satellite in the polar regions and at mid-latitudes, but in the tropics the GEOS-Chem BrO is too low by a factor of 2–4 throughout the year (Fig. 5 of Parrella et al., 2012). Furthermore, recent aircraft-based observations of BrO in the tropical and subtropical free troposphere of the Southern Hemisphere reported concentrations which were 2–4 times higher than predicted by the GEOS-Chem model (Wang et al., 2015).

In the second sensitivity simulation (FastK), we replace the Donohoue et al. (2006) rate constant for Reaction (R1) by the faster rate constant measured by Ariya et al. (2002). Following Dibble et al. (2012), we proportionally increase the rate constant for the backward reaction (R2) as follows:

$$k_{1,\text{FastK}} = 3.6 \times 10^{-12} \times \left( \frac{[\mathrm{M}]_{T,p}}{[\mathrm{M}]_{273.15\,\mathrm{K},1\,\mathrm{atm}}} \right) \quad \mathrm{cm}^{-3}\,\mathrm{molecule}^{-1}\,\mathrm{s}^{-1}$$

(Ariya et al., 2002) $\hspace{8cm}$ (5)

$$k_{2,\text{FastK}} = k_2 \times \left( \frac{k_{1,\text{FastK}}}{k_1} \right) \quad \mathrm{s}^{-1} \quad \text{(Goodsite et al., 2012, Dibble et al., 2012)} \hspace{2cm} (6)$$

Relative to the BASE simulation, $k_{1,\text{FastK}}$ and $k_{2,\text{FastK}}$ are 10 times larger near the surface and 5 times larger in the upper troposphere (10–12 km). For both these sensitivity simulations, the in-cloud reduction rate is increased such that the tropospheric burden and lifetime of THg is similar to the BASE simulation. This enables us to isolate the model's sensitivity to the redox chemistry of Hg.

At the 39 global land-based sites considered previously by Holmes et al. (2010), the results of the BASE ($1.71\,\mathrm{ng\,m}^{-3}$), $3\times$Br ($1.74\,\mathrm{ng\,m}^{-3}$), and FastK ($1.64\,\mathrm{ng\,m}^{-3}$) models are comparable to the

observations ($1.86\,\mathrm{ng\,m^{-3}}$). Figure S1 (in the Supplement) shows a comparison with observations
of the inter-hemispheric gradient and the seasonal cycle of total gaseous Hg concentrations.

### 3   Observed horizontal and vertical distribution of THg and Hg(II)

The vertical and horizontal distributions of THg and Hg(II) concentrations observed during
NOMADSS are presented in Figs. 2 and 3. We exclude from these figures and the rest of our anal-
ysis fresh pollution plumes, where $NO_x$, $SO_2$, or $C_3H_8$ exceed $2\,\mathrm{ppbv}$. This eliminates $6\,\%$ of the
THg and $4\,\%$ of the Hg(II) measurements. The mean and standard deviation of the observed THg
concentrations was $1.49\pm0.16\,\mathrm{ng\,m^{-3}}$ (Fig. 3a). THg concentrations decrease slightly with altitude,
from $1.54\,\mathrm{ng\,m^{-3}}$ near the surface to $1.38\,\mathrm{ng\,m^{-3}}$ at $6$–$7\,\mathrm{km}$ altitude (Fig. 2a), which is in agree-
ment with previous aircraft-based measurements of THg over North America (Talbot et al., 2007;
Swartzendruber et al., 2009; Mao et al., 2010). The variability in THg concentration is small, with
standard deviations at different levels ranging from 6 to $15\,\%$ of the mean concentrations. The weak
vertical gradient and the low standard deviation of the THg concentrations are consistent with the
long tropospheric lifetime of THg.

For Hg(II), the observed mean concentration was $212\pm112\,\mathrm{pg\,m^{-3}}$, for ADL measurements
($35\,\%$ of measurements) (Table 2̶3). When we include BDL values using the ROS method (see
Sect. 2.2), the mean Hg(II) concentration is $110\pm103\,\mathrm{pg\,m^{-3}}$ (Table 2̶3). In order to assess the
overall mean distribution of Hg(II) during NOMADSS, Figs. 2b and 3c display the Hg(II) statistics
that include BDL values estimated with the ROS method. Figure 2b shows that observed Hg(II) con-
centrations increased from $40\,\mathrm{pg\,m^{-3}}$ at $0$–$1\,\mathrm{km}$ altitude to $200\,\mathrm{pg\,m^{-3}}$ at $6$–$7\,\mathrm{km}$ (Fig. 2b). Large
enhancements in Hg(II) concentrations, of up to $500\,\mathrm{pg\,m^{-3}}$, were observed at $5$–$7\,\mathrm{km}$ during two
research flights (RF) over Texas (RF-06 and RF-09, box 1 in Figs. 2b and 3d). Concentrations of
up to $680\,\mathrm{pg\,m^{-3}}$ were observed at $1$–$3\,\mathrm{km}$ on one flight over the Atlantic Ocean (RF-16). We will
discuss these flights in more detail in Sect. 6.

Previous Hg(II) measurements at high-elevation ground sites and from aircraft showed that high
free tropospheric Hg(II) concentrations were generally observed in air masses that were dry and
clean (Landis et al., 2005; Swartzendruber et al., 2006, 2009; Fain et al., 2009; Sheu et al., 2010). To
examine whether this relation holds for the NOMADSS observations, we classify all THg and Hg(II)
observations based on the measured relative humidity (RH) and CO concentrations (Table 2̶3). We
use thresholds of $RH = 35\,\%$ and $CO = 75\,\mathrm{ppbv}$ to classify the observations into four categories:
"high RH/high CO", "high RH/low CO", "low RH/high CO", and "low RH/low CO". When RH or
CO measurements were not available ($18\,\%$ of the observations), we use the GEOS-Chem simulated
RH values and CO concentrations. The ROS procedure is used to assign values for BDL observations
separately for each category.

Using this method, Hg(II) observations partition into the four categories as follows (Table ~~2~~3): "low RH/low CO" (12 % of observations), "low RH/high CO" (28 %), "high RH/low CO" (10 %), "high RH/high CO" (50 %). The highest mean concentrations of Hg(II) are found in the "low RH/low CO" category (239 pg m$^{-3}$ for all observations, 289 pg m$^{-3}$ for ADL observations). Observations in this category had the lowest average THg concentrations (1.35 ng m$^{-3}$), and were relatively clean with low mixing ratios for CH$_2$O (0.5 ppbv), NO$_x$ (55 pptv), O$_3$ (52 ppbv), and a mean RH of 16 %. These air samples were observed mainly during the high altitude (5–7 km) flights over Texas (RF-06 and RF-09), and at 1–3 km over the Atlantic on RF-16. The chemical characteristics and HYbrid Single-Particle Lagrangian Integrated Trajectory (HYSPLIT) (Draxler and Hess, 1998) back trajectories for these "low RH/low CO" air masses indicate subsidence from the clean subtropical upper troposphere (Sect. 6).

The "low RH/high CO" category displays moderate enhancements in Hg(II) concentrations, with a mean of 146 pg m$^{-3}$ (189 pg m$^{-3}$ for ADL observations). Back trajectories (not shown here) indicate transport from high latitudes ($> 60°$ N) accompanied by subsidence. The mean concentrations of NO$_x$ (67 pptv) and CH$_2$O (0.7 ppbv) were low and similar to values for the "low RH/low CO" category, indicating relatively clean air masses but originating from the mid- and upper-troposphere at high latitudes instead of tropical latitudes as in the "low RH/low CO" category.

Most of the remaining Hg(II) observations (50 % of observations) fall in the "high RH/high CO" category. These observations were collected mainly in the continental boundary layer, with moderately high concentrations of CO (124 ppbv), CH$_2$O (2.7 ppbv), and NO$_x$ (232 pptv). In this category, the mean concentration of THg is 1.53 ng m$^{-3}$, while that of Hg(II) is 48 pg m$^{-3}$ (155 pg m$^{-3}$ for ADL observations, which account for only 14 % of observations in this category).

The "high RH/low CO" category has lower CO (68 ppbv), CH$_2$O (0.9 ppbv), NO$_x$ (44 pptv), and O$_3$ (43 ppbv). These samples were observed mostly near the marine boundary layer over the Atlantic Ocean (RF-14 and RF-16), but some were observed at high altitudes possibly in air detrained from clouds. In this category, the mean concentration of THg is 1.44 ng m$^{-3}$, and that of Hg(II) is 108 pg m$^{-3}$ (249 pg m$^{-3}$ for ADL observations, 30 % of the observations).

The observations of Hg(II) during NOMADSS are similar to previous observations of Hg(II) in terms of their magnitude, vertical profiles, and airmass characteristics. During five summertime flights in the Pacific Northwest, Swartzendruber et al. (2009) also found RGM (gaseous component of Hg(II)) to be generally below the instrument's DL of 80–160 pg m$^{-3}$. They found high RGM air masses (200–500 pg m$^{-3}$) on two flights at 2–6 km altitude. These air masses had low aerosol extinction coefficient, indicating either larger production of RGM at higher altitudes or loss of RGM in the presence of aerosol particles (Swartzendruber et al., 2009). On 28 flights from August 2012 to June 2013, Brooks et al. (2014) found that mean RGM and PBM (particle-bound component of Hg(II)) concentrations at 0–6 km over Tennessee, USA were ~~34.4 and 29.6~~34 and 30 pg m$^{-3}$, respectively. ~~The highest~~ Highest concentrations on each flight were always observed at 2–4.5 km altitude. RGM

325  concentrations exhibited a minimum in the winter months and a maximum in the summer months. On one flight in June 2013, the vertical profile of RGM showed a steep increase from the surface ($\sim 5 \, \mathrm{pg \, m^{-3}}$) to 4 km altitude ($120 \, \mathrm{pg \, m^{-3}}$) followed by decrease between 4 and 6 km ($70 \, \mathrm{pg \, m^{-3}}$) (Brooks et al., 2014). At the high elevation Mt. Bachelor Observatory (2.7 km a.s.l.) in Oregon, the mean RGM concentration during May–August 2005 was $43 \, \mathrm{pg \, m^{-3}}$ (Swartzendruber et al., 2006).

330  Low RGM concentrations ($< 50 \, \mathrm{pg \, m^{-3}}$) were seen in boundary layer air during the day, and higher concentrations were seen in free-tropospheric air during the night. The highest 10 % of nighttime RGM concentrations were between 160 and $600 \, \mathrm{pg \, m^{-3}}$, and were measured in air with low RH and low CO, in similarity to the observations of high Hg(II) in our "low RH/low CO" category during NOMADSS.

## 4  Comparison to the BASE GEOS-Chem Hg simulation

335

~~The~~ THg concentrations simulated in the BASE GEOS-Chem model ($1.51 \pm 0.08 \, \mathrm{ng \, m^{-3}}$) agree well with observations ($1.49 \pm 0.16 \, \mathrm{ng \, m^{-3}}$) (Fig. 3a–b). The model captures the lower THg concentrations observed over central Texas, South Carolina, and part of the Atlantic Ocean, but overestimates THg concentrations over the Ohio River Valley by $\sim 20 \, \%$, possibly because of recent reductions in

340  power plant emissions of mercury not captured in the 2011 NEI inventory used in our study. The model reproduces the vertical profile of observed THg, decreasing from $1.57 \, \mathrm{ng \, m^{-3}}$ (observed: $1.54 \pm 0.15 \, \mathrm{ng \, m^{-3}}$) near the surface to $1.43 \, \mathrm{ng \, m^{-3}}$ (observed: $1.38 \pm 0.19 \, \mathrm{ng \, m^{-3}}$) at 6–7 km altitude. However, we note that the variability of modeled THg in each 1 km bin (shaded green area in Fig. 2a) is a factor of 2 to 5 lower than the observed variability. Overall, the GEOS-Chem THg

345  concentrations are within $\pm 10 \, \%$ of the measured concentrations for 70 % of the observations, which indicates that the model provides reasonable simulations of the emissions and mean lifetime of THg in the lower and middle troposphere during NOMADSS.

Because the majority of Hg(II) measurements are below the $58$–$228 \, \mathrm{pg \, m^{-3}}$ DL of the UW-DOHGS instrument, we consider ADL and BDL observations separately. Table ~~3~~ 4 shows that when

350  observed Hg(II) are BDL (65 % of measurements), the mean Hg(II) concentrations predicted with the BASE simulation ($39 \pm 34 \, \mathrm{pg \, m^{-3}}$) are indeed below the instrument's DL. For ADL observations, the BASE model underestimates observations by a factor of 3 (model: $67 \pm 44 \, \mathrm{pg \, m^{-3}}$, observations: $212 \pm 112 \, \mathrm{pg \, m^{-3}}$). The model predicts an increase in Hg(II) concentrations with altitude which is much smaller than observed (Fig. 2b). While underestimating the observed mean concentrations, the

355  model captures the factor of 3–6 increase in Hg(II) in the "low RH" air mass categories relative to the "high RH" categories (Tables 2 and 3).

Figure 5 shows scatter plots between observed and modeled Hg(II) concentrations for the "low RH/low CO" and "low RH/high CO" categories. We find that the GEOS-Chem BASE simulation has a large negative ($-47$ to $-58 \, \%$) normalized mean bias (NMB $= \sum_i (M_i - O_i) / \sum_i O_i$), where

360     $O_i$ and $M_i$ are observed and simulated values, and for $O_i < \mathrm{DL}$, $\sum_i O_i$ is calculated using the ROS procedure). Furthermore, about 60 % of modeled Hg(II) values are within a factor of two of the observations (FAC2 = fraction of points where $0.5 \le M_i/O_i \le 2$, for $O_i \le \mathrm{DL}$, we assume $0.5 \le M_i/O_i \le 2$ if $M_i < 2 \times \mathrm{DL}$). If we consider only ADL observations, FAC2 decreases to 28–39 %.

    Figure S2 (Supplement) displays scatterplots for the "high RH" categories. For ADL observations,
365 the NMB is between $-75$ and $-94$ % for these categories (Fig. S2 and Table 34). We note that for these two "high RH" categories a conclusive evaluation of the model performance is difficult, however, because of the large fraction of BDL observations.

    Considering the systematic model underestimate of observed Hg(II) concentrations, particularly in dry air masses where reduction and wet deposition are suppressed, we hypothesize that the bias
370 in the Hg(II) concentrations is because the model simulated oxidation of Hg(0) to Hg(II) is too slow. We test this hypothesis in the next section by examining two sensitivity simulations.


## 5   Sensitivity studies with enhanced Hg(0) oxidation

    As described in Sect. 2.3.4, we conduct two sensitivity simulations: in the 3×Br simulation, we evaluate the model's response to an increase in Br concentrations, and in the FastK simulation, we
375 evaluate the model's response to a faster oxidation rate constant. The results of these simulations are summarized in Table 3 4 and detailed comparisons to observations are presented in Figs. 4 and 5. Both the 3×Br and FastK simulations reproduce the observed mean concentration (Table 34) and vertical profile (Fig. 4a) of THg as we compensate the increase in Hg(0) oxidation with an increase in Hg(II) reduction rate to maintain the THg burden.

380     The 3×Br and FastK simulations predict a stronger vertical gradient in Hg(II) concentrations, in closer agreement with observations (Fig. 4). Above $5 \, \mathrm{km}$, Hg(II) concentrations in the 3×Br ($165 \pm 104 \, \mathrm{pg \, m^{-3}}$) and FastK ($184 \pm 156 \, \mathrm{pg \, m^{-3}}$) simulations show significantly better agreement with observations ($189 \pm 103 \, \mathrm{pg \, m^{-3}}$) relative to the BASE simulation ($97 \pm 46 \, \mathrm{pg \, m^{-3}}$) (Fig. 4b). For the "low RH/low CO" category, average modeled Hg(II) concentrations increase from $99 \pm 48 \, \mathrm{pg \, m^{-3}}$
385 (BASE) to $162 \pm 104 \, \mathrm{pg \, m^{-3}}$ (3×Br) and $208 \pm 144 \, \mathrm{pg \, m^{-3}}$ (FastK), compared to the observed $239 \pm 141 \, \mathrm{pg \, m^{-3}}$. The modeled NMB for all Hg(II) observations in the "low RH/low CO" category decreases from $-58$ % (BASE simulation) to $-32$ % (3×Br) and $-12$ % (FastK), while the FAC2 index increases from 62 % (BASE) to 69 % (3×Br) and 80 % (FastK)(Fig. 5a and b, c). However, the sensitivity simulations cannot reproduce the high Hg(II) concentrations observed on RF-16 at
390 $1$–$3 \, \mathrm{km}$ (orange circles in Fig. 5). We present a detailed discussion of this flight in Sect. 6.

    In the "low RH/high CO" category, the 3×Br Hg(II) concentrations ($91 \pm 67 \, \mathrm{pg \, m^{-3}}$) are $\sim 20$ % higher than the BASE model ($76 \pm 36 \, \mathrm{pg \, m^{-3}}$), but lower than the observed concentrations ($146 \pm 81 \, \mathrm{pg \, m^{-3}}$) (Table 34). In the FastK simulation, Hg(II) concentrations increase to $128 \pm 95 \, \mathrm{pg \, m^{-3}}$, improving the NMB (FastK: $-11$ %, 3×Br: $-37$ %, BASE: $-47$ %) (Fig. 5d–f). For this category,

395 the $3\times$Br Hg(II) concentrations are not much higher than the BASE simulation because in the $3\times$Br

we use higher Br concentration only between $45°$ N and $45°$ S, whereas most of the "low RH/high

CO" air masses originated from high latitudes. The FAC2 index is higher in the FastK simulation

($75\%$) compared to the BASE ($58\%$) and $3\times$Br ($61\%$) simulations.

Overall, the factor of 2 decrease in model bias for Hg(II) with the sensitivity simulations par-

400 ticularly for the "low RH/low CO" air samples suggests that the oxidation of Hg(0) in the upper

troposphere is 3 ($3\times$Br) to 5 (FastK) times faster than what was considered previously in the GEOS-

Chem model.

We ran two additional simulations that included oxidation by OH/O$_3$ and by BrO, respectively,

in addition to the Br-initiated oxidation of the BASE version, to test whether the underestimate in

405 the modeled oxidation results from exclusion of these oxidants. We add the following oxidation

reactions to the model:

$$Hg(0) + O_3 \rightarrow Hg(II) \tag{R5}$$

$$Hg(0) + OH \rightarrow Hg(II) \tag{R6}$$

$$Hg(0) + BrO \rightarrow Hg(II) \tag{R7}$$

410 where $k_5 = 3.0 \times 10^{-20}\,\mathrm{cm^3\,molecule^{-1}\,s^{-1}}$ (Hall, 1995), $k_6 = 8.7 \times 10^{-14}\,\mathrm{cm^3\,mole-}$

$\mathrm{cule^{-1}\,s^{-1}}$ (Sommar et al., 2001), and $k_7 = 3.0 \times 10^{-14}\,\mathrm{cm^3\,molecule^{-1}\,s^{-1}}$ (Spicer et al.,

2002)

The inclusion of Hg(0) + O$_3$ and Hg(0) + OH pathways decreases the global tropospheric chem-

ical lifetime of Hg(0) for June–July 2013 from 3.2 months (BASE simulation) to 0.6 months, which

415 is also lower than the lifetimes in the $3\times$Br (1.9 months) and the FastK (0.7 months) simulations.

However, the Hg(0) + O$_3$ and Hg(0) + OH reaction pathways have a relatively small effect on the

modeled Hg(II) concentrations in the upper troposphere. The 5–7 km Hg(II) concentrations in this

simulation ($108 \pm 79\,\mathrm{pg\,m^{-3}}$) are similar to the BASE simulation ($97 \pm 45\,\mathrm{pg\,m^{-3}}$), but the Hg(II)

concentrations below 5 km ($71 \pm 51\,\mathrm{pg\,m^{-3}}$) are higher than the BASE simulation ($39 \pm 33\,\mathrm{pg\,m^{-3}}$).

420 The increase in oxidation with the Hg(0) + O$_3$ and Hg(0) + OH pathways is mostly in the lower

troposphere, whereas in the upper troposphere, faster oxidation is compensated by faster reduction.

While the oxidation rates of Hg(0) + O$_3$ and Hg(0) + OH reactions have large uncertainties (see

Sect. 1), our results indicate that the underestimate in Hg(II) concentrations in the BASE model

persists despite the inclusion of the Hg(0) + O$_3$ and Hg(0) + OH oxidation pathways.

425 When the Hg(0) + BrO oxidation pathway is added, the June–July global tropospheric chemical

lifetime of Hg(0) is 0.9 months. The simulated 5–7 km Hg(II) concentrations ($115 \pm 75\,\mathrm{pg\,m^{-3}}$) are

higher than those in the BASE simulation, but not as high as the $3\times$Br and FastK simulations, and

much lower than the observations. The NMB for the "low RH/low CO" air masses is $-47\%$ for

this simulation, compared to $-32\%$ for the $3\times$Br simulation and $-12\%$ for the FastK simulation.

430 Thus, although including the Hg(0) + BrO reaction with the rate from Spicer et al. (2002) brings the

model closer to the observations, it does not completely explain the model underestimate of Hg(II) concentrations.

## 6 Case studies of individual flights

We analyze in more detail three NOMADSS flights during which high concentrations of Hg(II) were observed. For RF-06 and RF-09 over Texas, we trace the origin of the high Hg(II) to transport from the subtropical Pacific anticyclone, while for RF-16 off the South Carolina Coast, enhanced Hg(II) concentrations appear to have been produced in the subtropical Atlantic anticyclone. The timeseries of the observations and model results along the flight tracks are shown in Figs. 6–8.

### 6.1 RF-06 (19 June 2013) and RF-09 (24 June 2013)

One of the goal of RF-06 was to sample in dry air masses with potentially enhanced Hg(II) concentrations. The meteorological forecasts indicated the presence of such an air mass at $6 \, \mathrm{km}$ altitude over west Texas. After sampling in the boundary layer, the aircraft ascended to $6.8 \, \mathrm{km}$ altitude, measuring $182–347 \, \mathrm{pg \, m^{-3}}$ of Hg(II) between 18:02 and 19:47 UTC (Fig. 6a and d). Hg(II) DL on this flight was $114 \, \mathrm{pg \, m^{-3}}$, and quartz wool was used as the Hg(II) filter on the instrument's Hg(0) channel. The mean concentration of THg in this air mass was $1.35 \, \mathrm{ng \, m^{-3}}$, about $20 \, \%$ lower that the THg concentrations measured during the rest of the flight (Fig. 6b). The observed low RH ($11 \, \%$), CO ($65 \, \mathrm{ppbv}$), $O_3$ ($39 \, \mathrm{ppbv}$), $NO_x$ ($53 \, \mathrm{pptv}$), $CH_2O$ ($204 \, \mathrm{pptv}$), and $C_3H_8$ ($36 \, \mathrm{pptv}$) indicate a clean and dry air mass (Fig. 6d). The $7 \, \mathrm{day}$ HYSPLIT back trajectories (Fig. 6e) indicate that the air mass was transported from the subtropical Pacific anticyclone $3 \, \mathrm{days}$ before it was sampled over Texas (see also Gratz et al., 2015a). The back trajectories show subsidence of the air mass from the upper troposphere ($10–12 \, \mathrm{km}$) before transport out of the Pacific anticyclone.

Figure 6c shows that the $3 \times \mathrm{Br}$ simulation captures the enhancement in Hg(II) concentrations observed over Texas (observations: $251 \, \mathrm{pg \, m^{-3}}$, $3 \times \mathrm{Br}$: $306 \, \mathrm{pg \, m^{-3}}$), while the BASE model ($146 \, \mathrm{pg \, m^{-3}}$) is too low and the FastK model ($367 \, \mathrm{pg \, m^{-3}}$) too high. Outside the region with the high Hg(II) concentration, all three model simulations calculate Hg(II) concentrations that are BDL(DL:114), and are in agreement with the observations. During this flight, observations indicate high BrO concentrations of $1.9 \pm 0.35 \, \mathrm{pptv}$ (Fig. 6d) (Gratz et al., 2015a). The GEOS-Chem modeled BrO concentrations in this air mass ($0.3–0.4 \, \mathrm{pptv}$) are a factor of 5 lower than the observations (Fig. 6d), and thus our assumption of higher Br concentrations in the $3 \times \mathrm{Br}$ simulation is more consistent with these measurements (Sect. 2.3.4).

The transport pattern of dry air from the subtropical Pacific upper troposphere to the southeastern US persisted for several days and was sampled again on 24 June 2013 during flight RF-09 (Fig. 7a). High Hg(II) concentrations of $200–480 \, \mathrm{pg \, m^{-3}}$ were measured between 16:00 and 19:30 UTC as the C-130 aircraft flew five constant-altitude legs between 2.5 and $6.7 \, \mathrm{km}$ over eastern Texas. Hg(II)

14

DL on this flight was 94 $pg\,m^{-3}$, and quartz wool was used as the Hg(II) filter. Low RH (19 %) and low $O_3$ concentrations (50 ppbv) accompanied the high Hg(II) (Fig. 7c and d). BrO measurements are not available for this flight due to interference of clouds with the instrument. The HYSPLIT back trajectories show transport from the subtropical Pacific anticyclone (Fig. 7e), similar to RF-06. As the C-130 aircraft descended to 1.2 km, high concentration of Hg(II) (up to 360 $pg\,m^{-3}$) were observed in the continental boundary layer between 19:30 and 20:00 UTC. This was associated with high THg concentrations of 2.0 $ng\,m^{-3}$, and was likely due to emissions of both Hg(II) and Hg(0) from nearby sources.

The mean THg concentrations for RF-09 calculated by the three simulations are between 1.38 and 1.42 $ng\,m^{-3}$, and are close to the mean of the observations (Fig. 7b). Between 16:00 and 19:00 UTC, the Hg(II) concentrations calculated with the FastK model (302 $pg\,m^{-3}$) are closer to the observations (321 $pg\,m^{-3}$) than with the BASE (127 $pg\,m^{-3}$) and 3×Br (253 $pg\,m^{-3}$) models (Fig. 7c). However, between 19:00 and 19:30 UTC, the modeled Hg(II) concentrations for the three simulations are considerably lower (40–60 $pg\,m^{-3}$) than the observed concentrations (300 $pg\,m^{-3}$). The simulated RH (54 %) during this time was also higher than the observed RH (25 %). A comparison of the observed and modeled vertical profiles of isoprene (not shown) indicates an overestimate in the modeled local boundary layer depth, which could explain the difference between the model and the observations for this section of the flight.

For both RF-06 and RF-09, the GEOS-Chem simulations predict that the high observed Hg(II) concentrations were produced in the upper troposphere of the Pacific anticyclone. The upper troposphere is characterized by fast oxidation of Hg(0) to Hg(II) due to cold temperatures and higher Br concentrations. Furthermore, the cloud-free conditions within the anticyclones prevent removal of Hg(II) by deposition and aqueous reduction, leading to accumulation of Hg(II) (Sect. 8).

### 6.2 RF-16 (8 July 2013)

During RF-16, the aircraft flew to the South Carolina coast, with the goal of measuring the vertical distribution of mercury over the ocean (Fig. 8a). Of the eight constant altitude legs flown over the Atlantic, four were in the free troposphere, between 1.0 and 4.5 km, and four were in the marine boundary layer (MBL). THg concentrations showed a slight decrease from the MBL (1.58 $ng\,m^{-3}$) to the top of the vertical profile (1.37 $ng\,m^{-3}$) (Fig. 8b). Hg(II) was mostly BDL (DL: 91 $pg\,m^{-3}$) in the MBL, but was high in the free troposphere reaching up to 680 $pg\,m^{-3}$ with a mean concentration of 450 $pg\,m^{-3}$(Fig. 8c). Hg(II) DL on this flight was 91 $pg\,m^{-3}$, and the Hg(II) filter was a cation exchange membrane.The free-tropospheric air had a low concentration of CO (65 ppbv) and low RH (33 %) (Fig. 8d). The $CHBr_3$ concentration was about 1 pptv in the free tropospheric air, compared to about 2 pptv in the MBL. In consistency with the low RH and $CHBr_3$, the HYSPLIT back trajectories show slow subsidence of the air mass from 4–6 km altitude in the subtropical Bermuda anticyclone (Fig. 8e).

The simulated THg concentrations in the MBL ($1.34$–$1.38\,\mathrm{ng\,m^{-3}}$) are lower than the observations ($1.58\,\mathrm{ng\,m^{-3}}$), suggesting an underestimate in the ocean emission flux (Song et al., 2015) or an overestimate in the deposition flux (Fig. 8b). None of the model simulations capture the enhancements in Hg(II) observed between 17:00 and 18:15 UTC, and again between 19:30 and 20:15 UTC (Fig. 8c). During this flight, observed BrO concentrations remained below the instrument's DL of $0.9\,\mathrm{pptv}$, and the modeled BrO concentrations were $0.1$–$0.3\,\mathrm{pptv}$. We performed an additional simulation increasing the modeled BrO concentrations in the free troposphere of the Bermuda anticyclone to $0.9\,\mathrm{pptv}$ (with a proportional increase in Br radical concentrations) for the FastK simulation (FastK + 0.9BrO). The resulting Hg(II) concentrations along the flight track increase to $150$–$500\,\mathrm{pg\,m^{-3}}$, in better agreement with the observations (Fig. 8c). The oxidation of Hg(0) in this air mass was considerably faster than the $3\times$Br or FastK simulations, which suggests that the uncertainties in both the Br radical concentrations and in the oxidation rate constant can simultaneously affect the overall bias in the modeled Hg(II) in certain areas.

## 7 Links to previous studies

The above comparison of the simulated Hg(II) concentrations with the NOMADSS observations shows that the Hg(0) oxidation based on the standard rate constants (Goodsite et al., 2004, 2012; Donohoue et al., 2006) and the GEOS-Chem calculated Br concentrations is too slow. Increasing the free tropospheric Br concentrations by a factor of 3 or considering the higher rate constants of Ariya et al. (2002) leads to significant improvement in the model results in the free troposphere compared to the NOMADSS observations. By contrast, Weiss-Penzias et al. (2015) found that the GEOS-Chem simulated Hg(II) concentrations in the free troposphere were 2.5 times higher on average than the observed concentrations at five high-elevation sites in western USA and Taiwan. Differences in the instruments and models used in their study and ours make it difficult to directly compare our findings. Weiss-Penzias et al. (2015) used the Tekran® 2537-1130-1135 system, which can underestimate Hg(II) in the presence of $O_3$ (Lyman et al., 2010; McClure et al., 2014). Their GEOS-Chem model is based on the reaction kinetics described in Holmes et al. (2010) and does not include updates described in Sect. 2.3.3. Importantly, the rate constant for the dissociation of HgBr (reaction R2) has since been corrected, and is now a factor of 10–20 higher than the previous value. The faster rate of dissociation of HgBr decreases the modeled Hg(II) concentration at $600\,\mathrm{hPa}$ by a factor of about 1.5.

The relatively high DL of the UW-DOHGS instrument make the NOMADSS observations unsuitable for an evaluation of faster oxidation in the boundary layer. However, three previous studies in the tropical and mid-latitude MBL have reported similar findings that the standard Hg(0) + Br oxidation kinetics are too slow to reproduce the observed Hg(II) concentrations, as discussed below.

16

Sprovieri et al. (2010) observed the diurnal cycle in RGM concentrations over the Adriatic Sea with daily enhancements of 20–40 $pg\,m^{-3}$ at midday. Using a box model, the authors found that they could reasonably reproduce the observations with the Ariya et al. (2002) rate constant for the $Hg(0) + Br$ reaction (R1), but only if the HgBr thermal dissociation (Reaction R2) was neglected. In their study, Br was considered to be the sole second-step oxidant (Reaction R4). If $HO_2$, $NO_2$, and BrO were to be included as second-step oxidants (Dibble et al., 2012), as we do in our FastK simulation, it would provide an additional pathway for the oxidation of HgBr to Hg(II), and partly overcome the slowing effect of the HgBr thermal dissociation.

In analyzing RGM observations over the Galapagos Islands in the equatorial Pacific, Wang et al. (2014) showed that the inclusion of $HO_2$ and $NO_2$ as second-step oxidants in the $Hg(0) + Br$ reaction scheme based on Goodsite et al. (2012) and Dibble et al. (2012) was necessary to simulate the observed magnitude of the midday peaks in RGM concentrations. The box modeling study assumed peak daytime BrO concentrations of 0.2 pptv, which is similar to the annual average GEOS-Chem BrO concentration of 0.14 pptv. However, because of the uncertainties in the Tekran® 2537-1130-1135 system measurements, the actual concentrations of Hg(II) could possibly be higher than the observed concentrations (Wang et al., 2014; Lyman et al., 2010; Ambrose et al., 2013).

Tas et al. (2012) present an analysis of mercury depletion events associated with extremely high BrO concentrations (20–80 pptv) over the Dead Sea in Israel. They found that the standard Br-initiated mechanism was insufficient to reproduce the rate of depletion of Hg(0) and showed that oxidation of Hg(0) by BrO, at a rate close to that reported by Spicer et al. (2002), was necessary to explain the loss of Hg(0). If the FastK kinetics are considered, the Br-initiated pathway by itself can explain a large fraction of observed depletion rate of Hg(0). Although, the BrO oxidation pathway cannot be entirely ignored (as discussed in Sect. 5), its importance, in this case, would be much smaller than found by Tas et al. (2012). Overall, these MBL studies are consistent with our analysis of the NOMADSS free tropospheric observations in implying much faster tropospheric oxidation of Hg(0) than currently assumed.

## 8 Implications of faster oxidation in the GEOS-Chem model

The global annual tropospheric mercury budgets for the three simulations are presented in Fig. 9. Despite faster oxidation in the $3\times Br$ and FastK simulations, we maintain the same global burden of THg by increasing the Hg(II) reduction rate (Sect. 2.3.4). Thus, the lifetime of THg against deposition is similar in all three simulations ($\sim$ 8.5 months). While we acknowledge that the modeled burden and lifetime of THg are affected by the uncertainty in the emission and deposition fluxes of mercury (Lin et al., 2006; Selin, 2009), we choose to maintain these in the three simulations because it allows us to focus on the model's sensitivity to redox kinetics.

The tropospheric oxidation of Hg(0) to Hg(II) increases from $10\,900\,\mathrm{Mg\,a^{-1}}$ in the BASE simulation, to $18\,300\,\mathrm{Mg\,a^{-1}}$ for $3\times$Br (factor of 1.7 increase) and $42\,100\,\mathrm{Mg\,a^{-1}}$ (factor of 3.9 increase) for the FastK simulation. The lifetime of Hg(0) against oxidation to Hg(II) decreases from 5 months in the BASE simulation to 2.8–1.2 months in the $3\times$Br and FastK simulations. The tropospheric burden of Hg(II) increases by 33 % in the $3\times$Br simulation and by 66 % in the FastK simulations.

Compared to the BASE simulation, the lifetime of Hg(II) against reduction decreases from 35 days (BASE simulation) to 19 days ($3\times$Br) and 8 days (FastK) simulations, respectively. This results in faster cycling between Hg(0) and Hg(II). Globally, 48 % of the Hg(II) formed in the troposphere in the BASE simulation is reduced back to Hg(0) (Fig. 9a), whereas in the $3\times$Br and FastK simulations, that fraction increases to 68–88 % (Fig. 9b and c). The faster reduction in the simulations with faster oxidation implies that reduction plays a predominant role in controlling the burden and distribution of Hg(II) in the atmosphere. In view of our poor understanding of Hg(II) reduction in the atmosphere (Subir et al., 2011), we suggest that further laboratory and field measurements be conducted to constrain this process.

In this study, we chose to increase the reduction rate of Hg(II) to maintain the global burden of THg when oxidation is enhanced in $3\times$Br and FastK simulations. An alternative approach would have been to keep the reduction rate constant and increase the global emissions of THg by factors of 2 to 4. Such a large increase exceeds the range of reported emission estimates (Selin, 2009; Song et al., 2015; Pirrone et al., 2010), and thus we did not consider it. Moreover, this would lead to a 2 to 4-fold decrease in the lifetime of THg against deposition which is not supported by the nearly constant vertical profiles of THg observed in the troposphere during NOMADSS and other aircraft campaigns (Holmes et al., 2010).

Figure 10 shows the simulated distribution of Hg(II) at $450\,\mathrm{hPa}$ ($6.5\,\mathrm{km}$) for 1 June-15 July 2013. In all three simulations, Hg(II) is enhanced in the subtropical anticyclones, with larger enhancements in the $3\times$Br and the FastK simulations (Fig. 10a–c). A vertical profile in the Pacific subtropical anticyclone (Box 1, Fig. 10d) shows that the increase occurs throughout the free troposphere (Fig. 10d). Over the eastern US (Fig. 10e), the free tropospheric Hg(II) vertical profiles are similar for the three simulations below $8\,\mathrm{km}$, where on average the increase in oxidation is matched by the increase in aqueous phase reduction in clouds. Above $8\,\mathrm{km}$, the absence of liquid clouds prevents reduction from compensating for faster oxidation, and Hg(II) concentrations in the $3\times$Br and FastK simulations are higher. Thus, the increase in the global Hg(II) mass burden in the $3\times$Br and FastK simulations is concentrated largely in the subtropical anticyclones, and, to a smaller extent, in the extra-tropical upper troposphere.

Two processes maintain the high modeled Hg(II) concentrations in the subtropical anticyclones. First, the anticyclones are characterized by large-scale sinking motion which transports higher Hg(II) concentrations from the upper troposphere where fast oxidation of Hg(0) results from higher Br concentrations and lower temperatures slowing the thermal dissociation of the HgBr intermediate

(Reaction R2). The locations of the $450\,\text{hPa}$ enhancements in Hg(II) concentrations displayed in Fig. 10 are thus largely associated with the descending branches of the Hadley circulation. Note that the model predicts larger Hg(II) concentrations in the Southern Hemisphere subtropics where the winter Hadley circulation is stronger. Second, the sinking air in the anticyclones suppresses cloud formation and precipitation, thereby preventing loss of Hg(II) by reduction and wet deposition. This leads to efficient accumulation of Hg(II) in the subtropical anticyclones, even at lower altitudes. The model predicts low $450\,\text{hPa}$ Hg(II) concentrations in regions in the tropics with high cloud cover and precipitation (such as the Western Pacific), and in regions with low insolation, such as the Southern (winter) Hemisphere polar region.

The model simulates frequent episodes of high Hg(II) concentrations at $6.5\,\text{km}$ over Texas during summer of 2013 (Fig. 11a). From 1 June to 15 July, simulated midday (noon-3 p.m.) Hg(II) concentrations were higher than $250\,\text{pg}\,\text{m}^{-3}$ for $15\,\text{days}$ in the FastK simulation ($3\times$Br: $12\,\text{days}$), two of which were the days when RF-06 and RF-09 were conducted. RF-10 also flew at $7\,\text{km}$ ($425\,\text{hPa}$) over northern Texas and Oklahoma (Fig. 1) on 27 June 2013, but observed Hg(II) concentrations remained BDL (DL: $134\,\text{pg}\,\text{m}^{-3}$) during the high altitude leg. The $3\times$Br and FastK modeled Hg(II) concentrations over this region during RF-10 were 136 and $208\,\text{pg}\,\text{m}^{-3}$, respectively, significantly lower than those simulated for RF-06 and RF-09. The highest Hg(II) at $6.5\,\text{km}$ over Texas and Oklahoma occurs when the wind over the southern US is southwesterly (Fig. 11b) transporting Hg(II) from the semi-permanent Pacific anticyclone, whereas the lowest concentrations occur when the transport is from the north (Fig. 11c). Our results suggest that the transport of Hg(II) produced in the Pacific anticyclone could be an important source of Hg(II) over southeastern US, potentially influencing wet deposition in the region if these high Hg(II) air masses are exposed to deep convection.

## 9 Conclusions

In this work, we have analyzed aircraft-based measurements of atmospheric mercury species (THg and Hg(II)) made during the NOMADSS campaign that took place over the southeastern US during summer 2013. The THg observations show a weak vertical gradient with higher concentrations in the bottom $1\,\text{km}$ ($1.54\,\text{ng}\,\text{m}^{-3}$), and lower concentrations between 6 and $7\,\text{km}$ ($1.38\,\text{ng}\,\text{m}^{-3}$) in the atmosphere.

During NOMADSS, the mean Hg(II) concentrations observed above the instrument's limit of detection was 212 ($\pm112$) $\text{pg}\,\text{m}^{-3}$. Using the robust regression on order statistics procedure, the estimated mean Hg(II) concentration for all observations was 110 ($\pm103$) $\text{pg}\,\text{m}^{-3}$. The highest Hg(II) concentrations, $300–680\,\text{pg}\,\text{m}^{-3}$, were seen at $5–7\,\text{km}$ altitude during two flights over Texas and at $1–3\,\text{km}$ during one flight over the Atlantic Ocean. These high Hg(II) concentrations were associated with clean subsiding air masses originating in the upper troposphere within the Pacific or Atlantic anticyclones. The low temperatures and high concentrations of the bromine radical in the upper tro-

posphere lead to faster oxidation of Hg(0), while the lack of removal from in-cloud reduction or wet deposition in the dry anticyclones lead to efficient accumulation of Hg(II).

We used the GEOS-Chem model to evaluate the oxidation kinetics and interpret these observations. The modeled THg concentrations are in close agreement with the observations, reproducing the horizontal and vertical distribution of THg. The simulated Hg(II) concentrations, on the other hand, are a factor of 2.2 lower than the observed concentrations. We attribute this systematic bias to an underestimate in the modeled oxidation of Hg(0) to Hg(II).

We perform two additional simulations with: (i) three times the Br radical concentrations between $45°$ N and $45°$ S and between $750\,\mathrm{hPa}$ and the tropopause ($3\times$Br), and (ii) a faster Hg(0) + Br oxidation rate constant (FastK). The model performance improves with both these simulations, especially above $5\,\mathrm{km}$ altitude and in air masses with low RH ($< 35\,\%$) and low CO ($< 75\,\mathrm{ppbv}$), where some of the highest Hg(II) concentrations were observed. For these air masses, the Hg(II) concentrations simulated with the $3\times$Br ($162\pm104\,\mathrm{pg\,m^{-3}}$) and the FastK ($208\pm144\,\mathrm{pg\,m^{-3}}$) models are 60–100 % higher than the BASE simulation ($99\pm48\,\mathrm{pg\,m^{-3}}$) and in closer agreement with the observations ($239\pm141\,\mathrm{pg\,m^{-3}}$). In addition to oxidation of Hg(0) by Br (BASE case), we considered the effect of including $O_3$ and OH as oxidants, but found that the high Hg(II) concentrations observed at 5-7 km could not be reproduced. We also examined the effect of adding the Hg(0)+BrO reaction to the BASE simulation, and found that the model underestimate of Hg(II) at 5-6 km persisted. Our modeling study suggests that the NOMADSS observations are most consistent with the $3\times$Br simulation and the FastK simulation, however we note that the relative importance of the different oxidation pathways cannot be ascertained before the chemical forms of Hg(II) in the atmosphere have been identified.

~~This faster~~ Faster oxidation decreases the lifetime of Hg(0) against oxidation from 5 months in the BASE simulation to 2.8 months with the $3\times$Br simulation, and to 1.2 month with the FastK simulation. To maintain the global THg burden, the faster modeled Hg(0) oxidation is balanced by an increase in the modeled Hg(II) reduction rates. The contribution of reduction to the overall loss of Hg(II) (by deposition and reduction) increases from 48 % in the BASE simulation to 68 and 88 % in the $3\times$Br and the FastK simulations, respectively, implying a greater importance of reduction to chemistry of mercury in the atmosphere. In the subtropical anticyclones, the $3\times$Br and FastK simulations predict a 3 to 5-fold enhancement in Hg(II) concentrations at $450\,\mathrm{hPa}$ relative to the global average Hg(II) concentration. These subtropical anticyclones are dry, cloud-free regions which provide ideal conditions for accumulation of Hg(II). The high Hg(II) in the Pacific anticyclone is periodically transported over southern US during summer and could be an important source of mercury wet deposition in the region. Future measurements in the subtropical anticyclones can help us gain deeper insights into the pathways of Hg(0) oxidation in the atmosphere.

**The Supplement related to this article is available online at doi:10.5194/acp-0-1-2016-supplement.**

## References

Ambrose, J. L., Lyman, S. N., Huang, J., Gustin, M. S., and Jaffe, D. A.: Fast time resolution oxidized mercury
measurements during the Reno Atmospheric Mercury Intercomparison Experiment (RAMIX), Environ. Sci.
Technol., 47, 7285–7294, doi:10.1021/es303916v, 2013.

Ambrose, J. L., Gratz, L. E., Jaffe, D. A., Campos, T., Flocke, F. M., Knapp, D. J., Stechman, D. M.,
Stell, M., Weinheimer, A., Cantrell, C., and Mauldin, R. L.: Mercury emission ratios from coal-fired power
plants in the southeastern U.S. during NOMADSS, Environ. Sci. Technol., 49, ~~10389--10397~~10389–10397,
doi:10.1021/acs.est.5b01755, 2015.

Amos, H. M., Jacob, D. J., Holmes, C. D., Fisher, J. A., Wang, Q., Yantosca, R. M., Corbitt, E. S., Galarneau, E.,
Rutter, A. P., Gustin, M. S., Steffen, A., Schauer, J. J., Graydon, J. A., Louis, V. L. St., Talbot, R. W.,
Edgerton, E. S., Zhang, Y., and Sunderland, E. M.: Gas-particle partitioning of atmospheric Hg(II) and its
effect on global mercury deposition, Atmos. Chem. Phys., 12, 591–603, doi:10.5194/acp-12-591-2012, 2012.

Amos, H. M., Jacob, D. J., Streets, D. G., and Sunderland, E. M.: Legacy impacts of all-time anthropogenic
emissions on the global mercury cycle, Global Biogeochem. Cy., 27, 410–421, doi:10.1002/gbc.20040, 2013.

Apel, E. C., Emmons, L. K., Karl, T., Flocke, F., Hills, A. J., Madronich, S., Lee-Taylor, J., Fried, A., Weibring,
P., Walega, J., Richter, D., Tie, X., Mauldin, L., Campos, T., Weinheimer, A., Knapp, D., Sive, B., Kleinman,
L., Springston, S., Zaveri, R., Ortega, J., Voss, P., Blake, D., Baker, A., Warneke, C., Welsh-Bon, D., de
Gouw, J., Zheng, J., Zhang, R., Rudolph, J., Junkermann, W., and Riemer, D. D.: Chemical evolution of
volatile organic compounds in the outflow of the Mexico City Metropolitan area, Atmos. Chem. Phys., 10,
2353–2375, doi:10.5194/acp-10-2353-2010, 2010.

Ariya, P. A., Khalizov, A., and Gidas, A.: Reactions of gaseous mercury with atomic and molecular
halogens: kinetics, product studies, and atmospheric implications, J. Phys. Chem. A, 106, 7310–7320,
doi:10.1021/jp020719o, 2002.

Balabanov, N. B., Shepler, B. C., and Peterson, K. A.: Accurate global potential energy surface and reaction
dynamics for the ground state of $HgBr_2$, J. Phys. Chem. A, 109, 8765–8773, doi:10.1021/jp053415l, 2005.

Bey, I., Jacob, D. J., Yantosca, R. M., Logan, J. A., Field, B. D., Fiore, A. M., Li, Q., Liu, H. Y., Mickley, L. J.,
and Schultz, M. G.: Global modeling of tropospheric chemistry with assimilated meteorology: model de-
scription and evaluation, J. Geophys. Res.-Atmos., 106, 23073–23095, doi:10.1029/2001jd000807, 2001.

Brooks, S., Ren, X., Cohen, M., Luke, W. T., Kelley, P., Artz, R., Hynes, A., Landing, W., and Martos, B.:
Airborne vertical profiling of mercury speciation near Tullahoma, TN, USA, Atmosphere, 5, 557–574,
doi:10.3390/atmos5030557, 2014.

Bullock, O. R., Atkinson, D., Braverman, T., Civerolo, K., Dastoor, A., Davignon, D., Ku, J.-Y., Lohman, K.,
Myers, T. C., Park, R. J., Seigneur, C., Selin, N. E, Sistla, G., and Vijayaraghavan, K.: The North American
Mercury Model Intercomparison Study (NAMMIS): study description and model-to-model comparisons, J.
Geophys. Res.-Atmos., 113, D17310, doi:10.1029/2008jd009803, 2008.

Bullock, O. R., Atkinson, D., Braverman, T., Civerolo, K., Dastoor, A., Davignon, D., Ku, J.-Y., Lohman, K.,
Myers, T. C., Park, R. J., Seigneur, C., Selin, N. E, Sistla, G., and Vijayaraghavan, K.: An analysis of sim-
ulated wet deposition of mercury from the North American Mercury Model Intercomparison Study, J. Geo-
phys. Res.-Atmos., 114, D08301, doi:10.1029/2008jd011224, 2009.

Calvert, J. G. and Lindberg, S. E.: Mechanisms of mercury removal by $O_3$ and OH in the atmosphere, Atmos. Environ., 39, 3355–3367, doi:10.1016/j.atmosenv.2005.01.055, 2005.

Dibble, T. S., Zelie, M. J., and Mao, H.: Thermodynamics of reactions of ClHg and BrHg radicals with atmo-
spherically abundant free radicals, Atmos. Chem. Phys., 12, 10271–10279, doi:10.5194/acp-12-10271-2012, 2012.

Donohoue, D. L., Bauer, D., Cossairt, B., and Hynes, A. J.: Temperature and pressure dependent rate coefficients for the reaction of Hg with Br and the reaction of Br with Br: a pulsed laser photolysis-pulsed laser induced fluorescence study, J. Phys. Chem. A, 110, 6623–6632, doi:10.1021/jp054688j, 2006.

Draxler, R. R. and Hess, G.: An overview of the HYSPLIT_4 modelling system for trajectories, Aust. Meteorol. Mag., 47, 295–308, 1998.

Driscoll, C. T., Mason, R. P., Chan, H. M., Jacob, D. J., and Pirrone, N.: Mercury as a global pollutant: sources, pathways, and effects, Environ. Sci. Technol., 47, 4967–4983, doi:10.1021/es305071v, 2013.

Ebinghaus, R., Kock, H. H., Temme, C., Einax, J. W., Löwe, A. G., Richter, A., Burrows, J. P., and Schroeder, W. H.: Antarctic springtime depletion of atmospheric mercury, Environ. Sci. Technol., 36, 1238–1244, doi:10.1021/es015710z, 2002.

Faïn, X., Obrist, D., Hallar, A. G., Mccubbin, I., and Rahn, T.: High levels of reactive gaseous mercury observed at a high elevation research laboratory in the Rocky Mountains, Atmos. Chem. Phys., 9, 8049–8060, doi:10.5194/acp-9-8049-2009, 2009.

Goodsite, M. E., Plane, J., and Skov, H.: A theoretical study of the oxidation of Hg0 to $HgBr_2$ in the troposphere, Environ. Sci. Technol., 38, 1772–1776, doi:10.1021/es034680s, 2004.

Goodsite, M. E., Plane, J., and Skov, H.: Correction to a theoretical study of the oxidation of Hg0 to $HgBr_2$ in the troposphere, Environ. Sci. Technol., 46, 5262–5262, doi:10.1021/es301201c, 2012.

Gratz, L. E., Shah, V., Ambrose, J. L., Jaffe, D. A., Jaeglé, L., Stutz, J., Festa, J., Selin, N. E., Song, S., Weinheimer, A. J., Knapp, D. J., Montzka, D. D., Campos, T. L., Flocke, F. M., Apel, E., Hornbrook, R., Blake, N. J., Hall, S., Tyndall, G. S., Reeves, M., Stechman, D., and Stell, M.: Oxidation of mercury by bromine in the subtropical pacific free troposphere, in prep. 2015a. Gratz, L. E., Ambrose, J. L., Jaffe, D. A., Shah, V., Jaeglé, L., Stutz, J., Festa, J., Spolaor, M., Tsai, C., Selin, N. E., Song, S., Zhou, X., Weinheimer, A. J., Knapp, D. J., Montzka, D. D., Flocke, F. M., Campos, T. L., Apel, E., Hornbrook, R., Blake, N. J., Hall, S., Tyndall, G. S., Reeves, M., Stechman, D., and Stell, M.: Oxidation of mercury by bromine in the subtropical Pacific free troposphere, Geophys. Res. Lett., 42, 10494–10502, doi:10.1002/2015GL066645, 2015a

Gratz, L. E., Ambrose, J. L., Jaffe, D. A., Knote, C., Jaeglé, L., Selin, N. E., Campos, T. L., Flocke, F. M., Reeves, M., Stechman, D., Stell, M., Weinheimer, A. J., Knapp, D. J., Montzka, D. D., Tyndall, G. S., Mauldin, R. L., Cantrell, C. A., Apel, E., Hornbrook, R., and Blake, N. J.: Airborne observations of mercury emissions from the Chicago/Gary Urban/Industrial Area during the 2013 NOMADSS Campaign, in prep. AGU Fall Meeting, San Francisco, USA, 14–18 December 2015, B11D-0457, 2015b.

Gustin, M. S., Huang, J., Miller, M. B., Peterson, C., Jaffe, D. A., Ambrose, J., Finley, B. D., Lyman, S. N., Call, K., Talbot, R., Feddersen, D., Mao, H., and Lindberg, S. E.: Do we understand what the mercury speciation instruments are actually measuring? Results of RAMIX, Environ. Sci. Technol., 47, 7295–7306, doi:10.1021/es3039104, 2013.

Hall, B.: The gas phase oxidation of elemental mercury by ozone, Water Air Soil Poll., 80, 301–315, doi:10.1007/bf01189680, 1995.

Helsel, D. R.: Statistics for Censored Environmental Data Using Minitab and R, John Wiley and Sons, Hoboken, NJ, USA, doi:10.1002/9781118162729, 2011.

Holmes, C. D., Jacob, D. J., and Yang, X.: Global lifetime of elemental mercury against oxidation by atomic bromine in the free troposphere, Geophys. Res. Lett., 33, L20808, doi:10.1029/2006gl027176, 2006.

Holmes, C. D., Jacob, D. J., Corbitt, E. S., Mao, J., Yang, X., Talbot, R., and Slemr, F.: Global atmospheric model for mercury including oxidation by bromine atoms, Atmos. Chem. Phys., 10, 12037–12057, doi:10.5194/acp-10-12037-2010, 2010.

Huang, J., Miller, M. B., Edgerton, E., and Gustin, M. S.: Use of criteria pollutants, active and passive mercury sampling, and receptor modeling to understand the chemical forms of gaseous oxidized mercury in Florida, Atmos. Chem. Phys. Discuss., 15, 12069–12105, doi:10.5194/acpd-15-12069-2015, 2015.

Hynes, A. J., Donohoue, D. L., Goodsite, M. E., and Hedgecock, I. M.: Our current understanding of major chemical and physical processes affecting mercury dynamics in the atmosphere and at the air-water/terrestrial interfaces, in: Mercury Fate and Transport in the Global Atmosphere, edited by: Mason, R. and Pirrone, N., Springer Science + Business Media, New York, NY, USA, 427–457, doi:10.1007/978-0-387-93958-2_14, 2009.

Karagas, M., Choi, A. L., Oken, E., Horvat, M., Schoeny, R., Kamai, E., Grandjean, P., and Korrick, S.: Evidence on the human health effects of low level methylmercury exposure, Environ. Health Persp., 120, 799–806, doi:10.3410/f.717797859.793302881, 2012.

Kos, G., Ryzhkov, A., Dastoor, A., Narayan, J., Steffen, A., Ariya, P. A., and Zhang, L.: Evaluation of discrepancy between measured and modelled oxidized mercury species, Atmos. Chem. Phys., 13, 4839–4863, doi:10.5194/acp-13-4839-2013, 2013.

Lamborg, C., Fitzgerald, W., Damman, A., Benoit, J., Balcom, P., and Engstrom, D.: Modern and historic atmospheric mercury fluxes in both hemispheres: global and regional mercury cycling implications, Global Biogeochem. Cy., 16, 51-1–51-11, doi:10.1029/2001gb001847, 2002.

Landis, M. S., Stevens, R. K., Schaedlich, F., and Prestbo, E. M.: Development and characterization of an annular denuder methodology for the measurement of divalent inorganic reactive gaseous mercury in ambient air, Environ. Sci. Technol., 36, 3000–3009, doi:10.1021/es015887t, 2002.

Landis, M. S., Lynam, M. M., and Stevens, R. K.: The monitoring and modelling of Hg species in support of local, regional and global modelling, in: Dynamics of Mercury Pollution on Regional and Global Scales:, edited by: Pirrone, N. and Mahaffey, K., Springer Science + Business Media, New York, NY, USA, 123–151, doi:10.1007/0-387-24494-8_7, 2005.

Laurier, F. J., Mason, R. P., Whalin, L., and Kato, S.: Reactive gaseous mercury formation in the North Pacific Ocean's marine boundary layer: a potential role of halogen chemistry, J. Geophys. Res.-Atmos., 108, 4529, doi:10.1029/2003JD003625, 2003.

Lin, C.-J., Pongprueksa, P., Lindberg, S. E., Pehkonen, S. O., Byun, D., and Jang, C.: Scientific uncertainties in atmospheric mercury models I: Model science evaluation, Atmos. Environ., 40, 2911–2928, 2006.

800    Lin, J.-T., and McElroy, M. B.: Impacts of boundary layer mixing on pollutant vertical profiles in the lower troposphere: implications to satellite remote sensing, Atmos. Environ., 44, 1726–1739, doi:10.1016/j.atmosenv.2010.02.009, 2010.

Lin, S.-J., and Rood, R. B.: Multidimensional flux-form semi-Lagrangian transport schemes, Mon. Weather Rev., 124, 2046–2070, doi:10.1175/1520-0493(1996)124<2046:MFFSLT>2.0.CO;2, 1996.

805    Lindberg, S. E., Brooks, S., Lin, C.-J., Scott, K. J., Landis, M. S., Stevens, R. K., Goodsite, M., and Richter, A.: Dynamic oxidation of gaseous mercury in the Arctic troposphere at polar sunrise, Environ. Sci. Technol., 36, 1245–1256, doi:10.1021/es0111941, 2002.

Liu, H., Jacob, D. J., Bey, I., and Yantosca, R. M.: Constraints from 210Pb and 7Be on wet deposition and transport in a global three-dimensional chemical tracer model driven by assimilated meteorological fields, J.

810    Geophys. Res.-Atmos., 106, 12109–12128, doi:10.1029/2000jd900839, 2001.

Lyman, S. N. and Jaffe, D. A.: Formation and fate of oxidized mercury in the upper troposphere and lower stratosphere, Nat. Geosci., 5, 114–117, doi:10.1038/ngeo1353, 2012.

Lyman, S. N., Jaffe, D. A., and Gustin, M. S.: Release of mercury halides from KCl denuders in the presence of ozone, Atmos. Chem. Phys., 10, 8197–8204, doi:10.5194/acp-10-8197-2010, 2010.

815    Mao, H., Talbot, R. W., Sive, B. C., Kim, S. Y., Blake, D. R., and Weinheimer, A. J.: Arctic mercury depletion and its quantitative link with halogens, J. Atmos. Chem., 65, 145–170, doi:10.1007/s10874-011-9186-1, 2010.

McClure, C. D., Jaffe, D. A., and Edgerton, E. S.: Evaluation of the KCl Denuder method for gaseous oxidized mercury using $HgBr_2$ at an in-service AMNet site, Environ. Sci. Technol., 48, 11437–11444,

820    doi:10.1021/es502545k, 2014.

Mergler, D., Anderson, H. A., Chan, L. H. M., Mahaffey, K. R., Murray, M., Sakamoto, M., and Stern, A. H.: Methylmercury exposure and health effects in humans: a worldwide concern, AMBIO, 36, 3–11, doi:10.1579/0044-7447(2007)36[3:MEAHEI]2.0.CO;2, 2007.

Obrist, D., Tas, E., Peleg, M., Matveev, V., Faïn, X., Asaf, D., and Luria, M.: Bromine-induced oxidation of

825    mercury in the mid-latitude atmosphere, Nat. Geosci., 4, 22–26, doi:10.1038/ngeo1018, 2011.

Pal, B. and Ariya, P. A.: Gas-phase HO-initiated reactions of elemental mercury: kinetics, product studies, and atmospheric implications, Environ. Sci. Technol., 38, 5555–5566, doi:10.1021/es0494353, 2004a.

Pal, B. and Ariya, P. A.: Studies of ozone initiated reactions of gaseous mercury: kinetics, product studies, and atmospheric implications, Phys. Chem. Chem. Phys., 6, 572–579, doi:10.1039/b311150d, 2004b.

830    Parrella, J. P., Jacob, D. J., Liang, Q., Zhang, Y., Mickley, L. J., Miller, B., Evans, M. J., Yang, X., Pyle, J. A., Theys, N., and Van Roozendael, M.: Tropospheric bromine chemistry: implications for present and pre-industrial ozone and mercury, Atmos. Chem. Phys., 12, 6723–6740, doi:10.5194/acp-12-6723-2012, 2012.

Pirrone, N., Cinnirella, S., Feng, X., Finkelman, R. B., Friedli, H. R., Leaner, J., Mason, R., Mukherjee, A. B., Stracher, G. B., Streets, D. G., and Telmer, K.: Global mercury emissions to the atmosphere from anthro-

835    pogenic and natural sources, Atmos. Chem. Phys., 10, 5951–5964, doi:10.5194/acp-10-5951-2010, 2010.

Ridley, B., Ott, L., Pickering, K., Emmons, L., Montzka, D., Weinheimer, A., Knapp, D., Grahek, F., Li, L., Heymsfield, G., McGill, M., Kucera, P., Mahoney, M. J., Baumgardner, D., Schultz, M., and Brasseur, G.: Florida thunderstorms: a faucet of reactive nitrogen to the upper troposphere, J. Geophys. Res.-Atmos., 109, D17305, doi:10.1029/2004JD004769, 2004.

840    Rienecker, M., Suarez, M. J., Todling, R., Bacmeister, J., Takacs, L., Liu, H., Gu, W., Sienkiewicz, M., Koster, R., Gelaro, R., Stajner, I., and Nielsen, J. E.: The GEOS-5 Data Assimilation System-Documentation of Versions 5.0. 1, 5.1. 0, and 5.2.0, NASA Tech. Rep, NASA/TM–2008–104606, Vol. 27, 2008.

Rutter, A., Shakya, K., Lehr, R., Schauer, J., and Griffin, R.: Oxidation of gaseous elemental mercury in the presence of secondary organic aerosols, Atmos. Environ., 59, 86–92, doi:10.1016/j.atmosenv.2012.05.009,
845    2012.

Scheuhammer, A. M., Meyer, M. W., Sandheinrich, M. B., and Murray, M. W.: Effects of environmental methylmercury on the health of wild birds, mammals, and fish, AMBIO, 36, 12–19, doi:10.1579/0044-7447(2007)36[12:EOEMOT]2.0.CO;2, 2007.

Selin, N. E.: Global biogeochemical cycling of mercury: a review, Annu. Rev. Env. Resour., 34, 43–63,
850    doi:10.1146/annurev.environ.051308.084314, 2009.

Selin, N. E., Jacob, D. J., Park, R. J., Yantosca, R. M., Strode, S., Jaeglé, L., and Jaffe, D.: Chemical cycling and deposition of atmospheric mercury: global constraints from observations, J. Geophys. Res.-Atmos., 112, D02308, doi:10.1029/2006jd007450, 2007.

Selin, N. E., Jacob, D. J., Yantosca, R. M., Strode, S., ~~Jaegle~~Jaeglé, L., and Sunderland, E. M.: Global 3-D land-
855    ocean-atmosphere model for mercury: present-day versus preindustrial cycles and anthropogenic enrichment factors for deposition, Global Biogeochem. Cy., 22, GB2011, doi:10.1029/2007GB003040, 2008.

Shepler, B. C., Balabanov, N. B., and Peterson, K. A.: $Hg + Br \rightarrow HgBr$ recombination and collision-induced dissociation dynamics, J. Chem. Phys., 127, 164304, doi:10.1063/1.2777142, 2007.

Sheu, G.-R., Lin, N.-H., Wang, J.-L., Lee, C.-T., Yang, C.-F. O., and Wang, S.-H.: Temporal distribution and
860    potential sources of atmospheric mercury measured at a high-elevation background station in Taiwan, Atmos. Environ., 44, 2393–2400, doi:10.1016/j.atmosenv.2010.04.009, 2010.

Sillman, S., Marsik, F. J., Al-Wali, K. I., Keeler, G. J., and Landis, M. S.: Reactive mercury in the troposphere: model formation and results for Florida, the northeastern United States, and the Atlantic Ocean, J. Geophys. Res.-Atmos., 112, D23305, doi:10.1029/2006jd008227, 2007.

865    Soerensen, A. L., Sunderland, E. M., Holmes, C. D., Jacob, D. J., Yantosca, R. M., Skov, H., Christensen, J. H., Strode, S. A., and Mason, R. P.: An improved global model for air-sea exchange of mercury: high concentrations over the North Atlantic, Environ. Sci. Technol., 44, 8574–8580, doi:10.1021/es102032g, 2010.

Sommar, J., Gårdfeldt, K., Strömberg, D., and Feng, X.: A kinetic study of the gas-phase reaction between the hydroxyl radical and atomic mercury, Atmos. Environ., 35, 3049–3054, doi:10.1016/s1352-2310(01)00108-
870    x, 2001.

Song, S., Selin, N., Jaffe, D., ~~Jaegle~~Jaeglé, L., Gratz, L., Ambrose, J., Shah, V., and Giang, A.: Use of NOMADSS Observations to Improve Our Understanding of the Land and Ocean Fluxes of Mercury, AGU Fall Meeting, San Francisco, USA, ~~14–18~~15–19 December 2014, A32A-07, 2014.

Song, S., Selin, N. E., Soerensen, A. L., Angot, H., Artz, R., Brooks, S., Brunke, E.-G., Conley, G., Dommer-
875    gue, A., Ebinghaus, R., Holsen, T. M., Jaffe, D. A., Kang, S., Kelley, P., Luke, W. T., Magand, O., Maru-moto, K., Pfaffhuber, K. A., Ren, X., Sheu, G.-R., Slemr, F., Warneke, T., Weigelt, A., Weiss-Penzias, P., Wip, D. C., and Zhang, Q.: Top-down constraints on atmospheric mercury emissions and implications for global biogeochemical cycling, Atmos. Chem. Phys., 15, 7103–7125, doi:10.5194/acp-15-7103-2015, 2015.

Spicer, C., Satola, J., Abbgy, A., Plastridge, R., and Cowen, K.: Kinetics of Gas-Phase Elemental Mercury Reactions with Halogen Species, Ozone, and Nitrate Radical under Atmospheric Conditions, Final report to Florida Department of Environmental Protection, 2002.

Sprovieri, F., Hedgecock, I. M., and Pirrone, N.: An investigation of the origins of reactive gaseous mercury in the Mediterranean marine boundary layer, Atmos. Chem. Phys., 10, 3985–3997, doi:10.5194/acp-10-3985-2010, 2010.

Strode, S. A., Jaeglé, L., Selin, N. E., Jacob, D. J., Park, R. J., Yantosca, R. M., Mason, R. P., and Slemr, F.: Air-sea exchange in the global mercury cycle, Global Biogeochem. Cy., 21, GB1017, doi:10.1029/2006gb002766, 2007.

Strode, S., Jaeglé, L., and Emerson, S.: Vertical transport of anthropogenic mercury in the ocean, Global Biogeochem. Cy., 24, GB4014, doi:10.1029/2009gb003728, 2010.

Subir, M., Ariya, P. A., and Dastoor, A. P.: A review of uncertainties in atmospheric modeling of mercury chemistry I. Uncertainties in existing kinetic parameters–Fundamental limitations and the importance of heterogeneous chemistry, Atmos. Environ., 45, 5664–5676, doi:10.1016/j.atmosenv.2011.04.046, 2011.

Sumner, A. L., Spicer, C. W., Satola, J., Mangaraj, R., Cowen, K. A., Landis, M. S., Stevens, R. K., and Atkeson, T. D.: Environmental chamber studies of mercury reactions in the atmosphere, in: Dynamics of Mercury Pollution on Regional and Global Scales, edited by: Pirrone, N. and Mahaffey, K., Springer Science + Business Media, New York, NY, USA, 193–212, doi:10.1007/0-387-24494-8_9, 2005.

Swartzendruber, P. C., Jaffe, D. A., Prestbo, E., Weiss-Penzias, P., Selin, N. E., Park, R., Jacob, D. J., Strode, S., and Jaeglé, L.: Observations of reactive gaseous mercury in the free troposphere at the Mount Bachelor Observatory, J. Geophys. Res.-Atmos., 111, D24301, doi:10.1029/2006jd007415, 2006.

Swartzendruber, P., Jaffe, D., and Finley, B.: Development and first results of an aircraft-based, high time resolution technique for gaseous elemental and reactive (oxidized) gaseous mercury, Environ. Sci. Technol., 43, 7484–7489, doi:10.1021/es901390t, 2009.

Talbot, R., Mao, H., Scheuer, E., Dibb, J., and Avery, M.: Total depletion of Hg in the upper troposphere–lower stratosphere, Geophys. Res. Lett., 34, L23804, doi:10.1029/2007gl031366, 2007.

Tas, E., Obrist, D., Peleg, M., Matveev, V., Faïn, X., Asaf, D., and Luria, M.: Measurement-based modelling of bromine-induced oxidation of mercury above the Dead Sea, Atmos. Chem. Phys., 12, 2429–2440, doi:10.5194/acp-12-2429-2012, 2012.

Tossell, J.: Calculation of the energetics for the oligomerization of gas phase HgO and HgS and for the solvolysis of crystalline HgO and HgS, J. Phys. Chem. A, 110, 2571–2578, doi:10.1021/jp056280s, 2006.

Travnikov, O., Lin, C., Dastoor, A., Bullock, O., Hedgecock, I., Holmes, C., Ilyin, I., Jaeglé, L., Jung, G., Pan, L., Pongprueksa, P., Ryzhkov, A., Seigneur, C., Skov, H.: Global and regional modeling, in: Hemispheric Transport of Air Pollutants (HTAP) Assessment Report. Part B: Mercury, edited by: Pirrone, N. and Keating, T., UN-Economic Commission for Europe, Geneva, 97–144, 2010.

Wang, F., Saiz-Lopez, A., Mahajan, A. S., Gómez Martín, J. C., Armstrong, D., Lemes, M., Hay, T., and Prados-Roman, C.: Enhanced production of oxidised mercury over the tropical Pacific Ocean: a key missing oxidation pathway, Atmos. Chem. Phys., 14, 1323–1335, doi:10.5194/acp-14-1323-2014, 2014.

Wang, Q., Jacob, D. J., Fisher, J. A., Mao, J., Leibensperger, E. M., Carouge, C. C., Le Sager, P., Kondo, Y., Jimenez, J. L., Cubison, M. J., and Doherty, S. J.: Sources of carbonaceous aerosols and deposited black

carbon in the Arctic in winter-spring: implications for radiative forcing, Atmos. Chem. Phys., 11, 12453–
12473, doi:10.5194/acp-11-12453-2011, 2011.

Wang, S., Schmidt, J. A., Baidar, S., Coburn, S., Dix, B., Koenig, T. K., Apel, E., Bowdalo, D., Campos, T. L.,
Eloranta, E., Evans, M. J., DiGangi, J. P., Zondlo, M. A., Gao, R.-S., Haggerty, J. A., Hall, S. R., Horn-
brook, R. S., Jacob, D., Morley, B., Pierce, B., Reeves, M., Romashkin, P., ter Schure, A., and Volkamer, R.:
Active and widespread halogen chemistry in the tropical and subtropical free troposphere, P. Natl. Acad. Sci.
USA, 112, 9281–9286, doi:10.1073/pnas.1505142112, 2015.

Wang, Y., Logan, J. A., and Jacob, D. J.: Global simulation of tropospheric $O_3-NO_x$-hydrocarbon chem-
istry: 2. Model evaluation and global ozone budget, J. Geophys. Res.-Atmos., 103, 10727–10755,
doi:10.1029/98jd00157, 1998.

Weiss-Penzias, P., Amos, H. M., Selin, N. E., Gustin, M. S., Jaffe, D. A., Obrist, D., Sheu, G.-R., and Giang, A.:
Use of a global model to understand speciated atmospheric mercury observations at five high-elevation sites,
Atmos. Chem. Phys., 15, 1161–1173, doi:10.5194/acp-15-1161-2015, 2015.

Wu, S., Mickley, L. J., Jacob, D. J., Logan, J. A., Yantosca, R. M., and Rind, D.: Why are there large differ-
ences between models in global budgets of tropospheric ozone?, J. Geophys. Res.-Atmos., 112, D05302,
doi:10.1029/2006jd007801, 2007.

Zhang, L., Jacob, D. J., Downey, N. V., Wood, D. A., Blewitt, D., Carouge, C. C., van Donkelaar, A.,
Jones, D. B., Murray, L. T., and Wang, Y.: Improved estimate of the policy-relevant background ozone in
the United States using the GEOS-Chem global model with $1/2 \times 2/3$ horizontal resolution over North
America, Atmos. Environ., 45, 6769–6776, doi:10.1016/j.atmosenv.2011.07.054, 2011.

Zhang, Y., Jaeglé, L., van Donkelaar, A., Martin, R. V., Holmes, C. D., Amos, H. M., Wang, Q., Talbot, R.,
Artz, R., Brooks, S., Luke, W., Holsen, T. M., Felton, D., Miller, E. K., Perry, K. D., Schmeltz, D., Steffen, A.,
Tordon, R., Weiss-Penzias, P., and Zsolway, R.: Nested-grid simulation of mercury over North America,
Atmos. Chem. Phys., 12, 6095–6111, doi:10.5194/acp-12-6095-2012, 2012.

Zhang, Y., Jaeglé, L., Thompson, L., and Streets, D. G.: Six centuries of changing oceanic mercury, Global
Biogeochem. Cy., 28, 1251–1261, doi:10.1002/2014gb004939, 2014.

**Table 1.** Chemical and meteorological measurements used in this work.

| Observations | Measurement technique | Instrument model/Reference |
|---|---|---|
| THg, Hg(0), and Hg(II) | Dual-channel CVAFS (UW-DOHGS) | Lyman and Jaffe (2012); Ambrose et al. (2013, 2015) |
| BrO | Differential Optical Absorption Spectroscopy | Platt and Stutz (2008) |
| RH | Chilled mirror hygrometry | Buck 1011C |
| CO | Vacuum-UV Resonance Fluorescence | Aero-Laser AL5001 |
| NO, $NO_2$, $O_3$ | $NO_2$ chemiluminescence | Ridley et al. (2004) |
| $CH_2O$, $CHBr_3$, $C_3H_8$ | Gas chromatography/mass spectrometry | Apel et al. (2010) |
| $SO_2$ | Pulsed fluorescence | Thermo Scientific Model 43i-TLE |

**Table 2.** Summary of GEOS-Chem simulations performed for this study.

| Simulation | Oxidants | Reaction rate constants ($\mathrm{cm^3\,molecule^{-1}\,s^{-1}}$) |
|---|---|---|
| | Main simulations | |
| BASE | Br (Concentrations from the GEOS-Chem full-chemistry simulation) | $\mathrm{Hg(0)} + \mathrm{Br} : k = 1.46 \times 10^{-32} \times \left(\frac{\mathrm{T}}{298}\right)^{-1.86} \times [\mathrm{M}]$ (Donohoue et al., 2006) |
| 3×Br | Br (Concentrations scaled by a factor of 3 in the region bounded by 45°S and 45°N, and 750 hPa and the tropopause.) | Same as BASE |
| FastK | Same as BASE | $\mathrm{Hg(0)} + \mathrm{Br} : k = 3.6 \times 10^{-12} \times \left(\frac{\mathrm{M_{T,p}}}{\mathrm{M_{273.15K,1atm}}}\right)$ (Ariya et al., 2002) |
| | Supplemental simulations | |
| FastK+0.9BrO | Same as FastK, except BrO concentrations in the free troposphere over the northwest Atlantic Ocean were increased to 0.9 pptv only for RF-16 simulation. | Same as FastK |
| BASE+OH/O$_3$ | Br, OH and O$_3$ (Concentrations from the GEOS-Chem full chemistry simulation) | $\mathrm{Hg(0)} + \mathrm{Br}$: same as BASE $\mathrm{Hg(0)} + \mathrm{O_3}$: $k = 3.0 \times 10^{-20}$ (Hall, 1995) $\mathrm{Hg(0)} + \mathrm{OH}$: $k = 8.7 \times 10^{-14}$ (Sommar et al., 2001) |
| BASE+BrO | Br and BrO (Concentrations from the GEOS-Chem full chemistry simulation) | $\mathrm{Hg(0)} + \mathrm{Br}$: same as BASE $\mathrm{Hg(0)} + \mathrm{BrO}$: $k = 3.0 \times 10^{-14}$ (Spicer et al., 2002) |

**Table 3.** Chemical characteristics of NOMADSS observations classified in four air mass categories.

| | All observations | low RH/low CO | low RH/high CO | high RH/low CO | high RH/high CO |
|---|---|---|---|---|---|
| No of THg observations[a] | 2381 | 233 | 551 | 212 | 1385 |
| THg observations (ng m$^{-3}$) | $1.49 \pm 0.16$ | $1.35 \pm 0.15$ | $1.48 \pm 0.11$ | $1.44 \pm 0.20$ | $1.53 \pm 0.15$ |
| No of Hg(II) observations[b] | 1503 | 184 | 414 | 159 | 746 |
| (ADL) | (528) | (132) | (244) | (47) | (105) |
| Hg(II) all observations (pg m$^{-3}$)[c] | $110 \pm 103$ | $239 \pm 141$ | $146 \pm 81$ | $108 \pm 123$ | $48 \pm 57$ |
| (ADL)[d] | $(212 \pm 112)$ | $(289 \pm 136)$ | $(189 \pm 76)$ | $(249 \pm 140)$ | $(155 \pm 73)$ |
| Altitude (km) | $2.6 \pm 1.9$ | $4.6 \pm 1.8$ | $3.9 \pm 1.2$ | $2.9 \pm 2.2$ | $1.7 \pm 1.5$ |
| RH (%) | $49 \pm 27$ | $16 \pm 10$ | $15 \pm 9$ | $68 \pm 17$ | $66 \pm 13$ |
| CO (ppbv) | $107 \pm 33$ | $65 \pm 4$ | $97 \pm 13$ | $65 \pm 3$ | $124 \pm 30$ |
| O$_3$ (ppbv) | $55 \pm 14$ | $52 \pm 16$ | $63 \pm 17$ | $43 \pm 16$ | $54 \pm 10$ |
| NO$_x$ (pptv) | $158 \pm 156$ | $55 \pm 32$ | $67 \pm 34$ | $44 \pm 39$ | $232 \pm 170$ |
| CH$_2$O (ppbv) | $1.8 \pm 1.4$ | $0.5 \pm 0.3$ | $0.7 \pm 0.3$ | $0.9 \pm 0.4$ | $2.7 \pm 1.3$ |

The four air mass categories are based on thresholds of RH = 35 % and CO = 75 ppbv. The mean and standard deviation for each category are indicated.

[a] Number of 2.5 min THg samples.

[b] Total number of 2.5 min Hg(II) samples, including samples below the detection limit (BDL). The number in parenthesis indicates the number of 2.5 min Hg(II) samples above the detection limit (ADL).

[c] Mean Hg(II) concentration and standard deviation for all observations, including BDL as estimated using the ROS method.

[d] Mean Hg(II) concentration and standard deviation for ADL observations.

**Table 4.** Modeled THg and Hg(II) concentrations in the three GEOS-Chem Hg simulations for the four air mass categories.

| | All observations | "low RH/low CO" | "low RH/high CO" | "high RH/low CO" | "high RH/high CO" |
|---|---|---|---|---|---|
| | Observed Hg(II) (pg m$^{-3}$) | | | | |
| All | $110 \pm 103$ | $239 \pm 141$ | $146 \pm 81$ | $108 \pm 123$ | $48 \pm 57$ |
| (ADL) | $212 \pm 112$ | $289 \pm 136$ | $189 \pm 76$ | $249 \pm 140$ | $155 \pm 73$ |
| | BASE model Hg(II) (pg m$^{-3}$) | | | | |
| All | $49 \pm 41$ | $99 \pm 48$ | $76 \pm 36$ | $20 \pm 25$ | $28 \pm 19$ |
| (ADL)[a] | $67 \pm 44$ | $96 \pm 51$ | $75 \pm 34$ | $14 \pm 18$ | $38 \pm 19$ |
| (BDL)[b] | $39 \pm 44$ | $105 \pm 37$ | $78 \pm 39$ | $22 \pm 27$ | $26 \pm 18$ |
| | $3 \times$Br model Hg(II) (pg m$^{-3}$) | | | | |
| All | $62 \pm 72$ | $162 \pm 104$ | $91 \pm 67$ | $28 \pm 41$ | $29 \pm 28$ |
| (ADL)[a] | $98 \pm 94$ | $176 \pm 116$ | $94 \pm 76$ | $19 \pm 30$ | $44 \pm 29$ |
| (BDL)[b] | $43 \pm 94$ | $124 \pm 47$ | $86 \pm 51$ | $31 \pm 45$ | $26 \pm 27$ |
| | FastK model Hg(II) (pg m$^{-3}$) | | | | |
| All | $80 \pm 98$ | $208 \pm 144$ | $128 \pm 95$ | $18 \pm 25$ | $34 \pm 32$ |
| (ADL)[a] | $125 \pm 120$ | $216 \pm 160$ | $128 \pm 89$ | $16 \pm 17$ | $55 \pm 42$ |
| (BDL)[b] | $55 \pm 120$ | $189 \pm 88$ | $129 \pm 102$ | $19 \pm 28$ | $31 \pm 28$ |
| | Observed THg (ng m$^{-3}$) | | | | |
| All | $1.49 \pm 0.16$ | $1.35 \pm 0.15$ | $1.48 \pm 0.11$ | $1.44 \pm 0.20$ | $1.53 \pm 0.15$ |
| | BASE model THg (ng m$^{-3}$) | | | | |
| All | $1.51 \pm 0.08$ | $1.43 \pm 0.06$ | $1.50 \pm 0.05$ | $1.40 \pm 0.03$ | $1.55 \pm 0.07$ |
| | $3 \times$Br model THg (ng m$^{-3}$) | | | | |
| All | $1.51 \pm 0.11$ | $1.40 \pm 0.09$ | $1.50 \pm 0.08$ | $1.36 \pm 0.04$ | $1.55 \pm 0.10$ |
| | FastK model THg (ng m$^{-3}$) | | | | |
| All | $1.52 \pm 0.09$ | $1.44 \pm 0.07$ | $1.52 \pm 0.06$ | $1.40 \pm 0.04$ | $1.55 \pm 0.08$ |

[a] Model values corresponding to ADL observations.

[b] Model values corresponding to BDL observations.
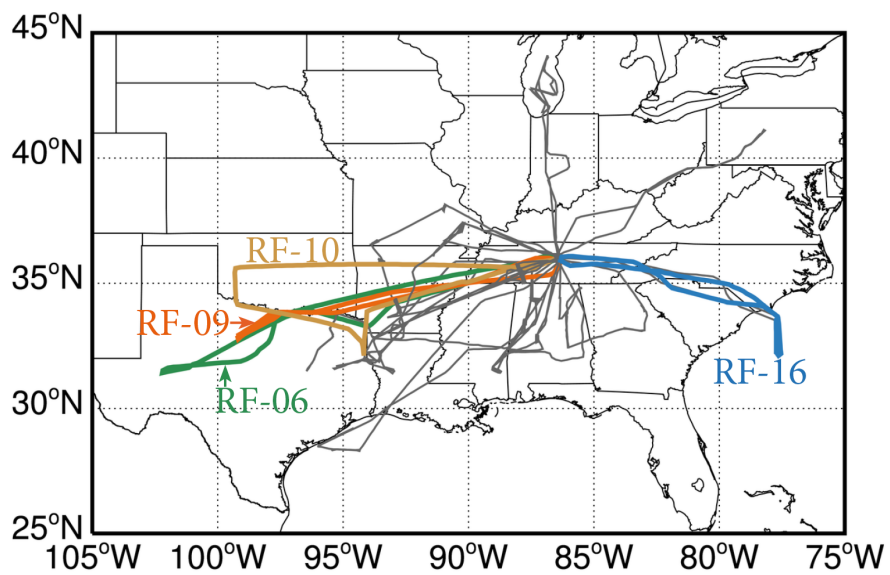
**Figure 1.** Flight tracks of the NSF/NCAR C-130 aircraft during the 19 NOMADSS research flights between 1 June and 15 July 2013. The flight tracks of four flights discussed in the text are highlighted ~~in color~~ (RF-06: green, RF-09: red, RF-10: brown, and RF-16: blue).
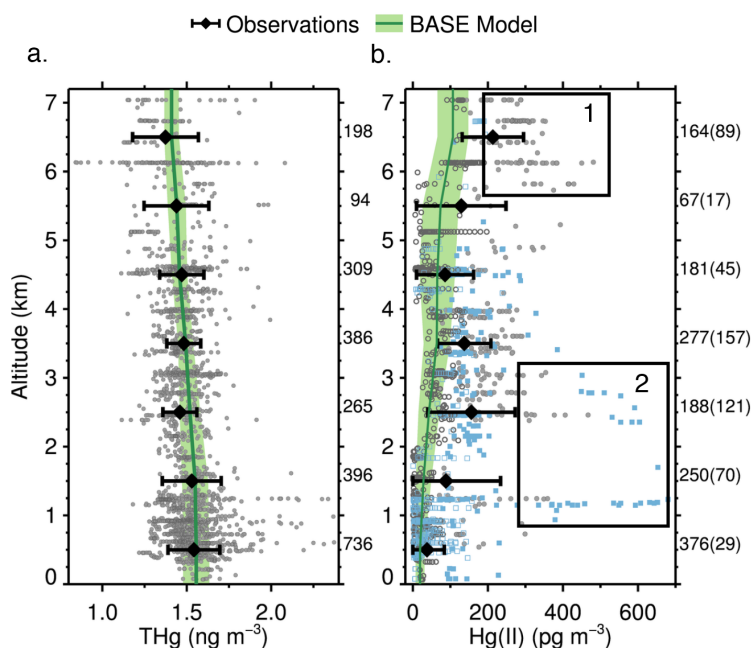
**Figure 2.** Vertical profiles of **(a)** THg and **(b)** Hg(II) during NOMADSS. Individual 2.5 min observations are shown with grey circles (for THg and Hg(II) measured using the quartz wool filter) and blue squares (for Hg(II) measured using the cation exchange membrane filter). Observations above the detection limit (ADL) are indicated as filled circles/squares, while observations below the detection limit (BDL) are as shown open circles/squares and are estimated using the regression on order statistics (ROS) method. The means and standard deviations calculated for 1 km vertical bins are shown for the observations (black diamonds and error bars) and the BASE GEOS-Chem simulation (green line and shading). The numbers on the right hand side of each panel indicate the number of 2.5 min observations in each 1 km bin. For Hg(II), the second number in parenthesis indicates the number of ADL observations. The areas marked as "1" and "2" highlight measurements of high Hg(II) concentrations and are referenced in the text and Fig. 3.
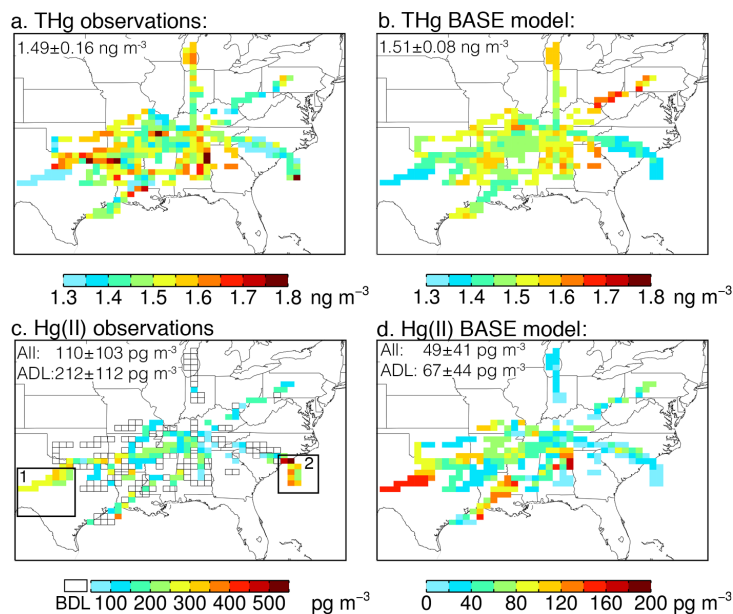
**Figure 3.** Horizontal distribution of THg (top panels) and Hg(II) (bottom panels). Observations are shown on panels **(a, c)**, while results from the BASE GEOS-Chem simulation are on panels **(b, d)**. Observed and simulated values are averaged in $0.5°$ latitude by $0.625°$ longitude columns. For Hg(II) observations, the means include ROS estimates for values below the detection limit (BDL). Locations where all observed Hg(II) concentrations were BDL are shown by open squares. Note the different color scales for the observed and modeled Hg(II) concentrations **(c, d)**. Regions marked as "1" and "2" highlight the areas with high Hg(II) and are referenced in the text and in Fig. 2. The numbers at the top of each panel indicate the means and standard deviations for all the modeled and observed concentrations. For Hg(II) we separate the statistics for all the measurements ("All") and for the measurements above the detection limit ("ADL").
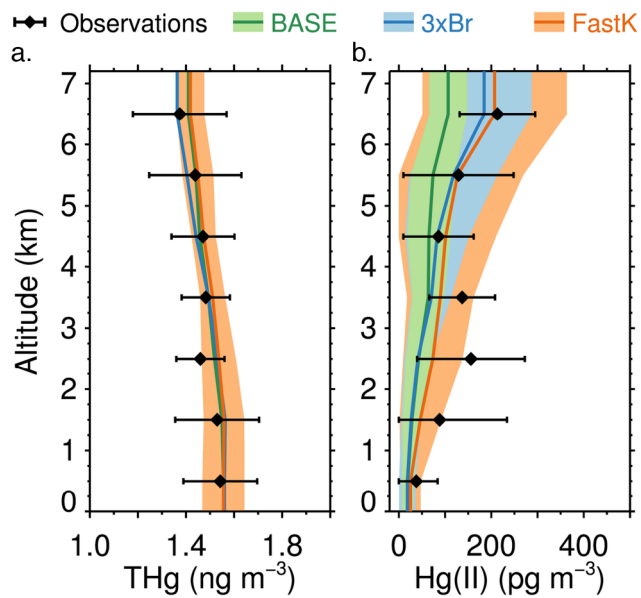
**Figure 4.** Mean vertical profiles of **(a)** THg and **(b)** Hg(II) concentrations averaged in 1 km vertical bins during NOMADSS. Observations are shown with black diamonds (error bars indicate the standard deviation). BDL Hg(II) observations are estimated using the ROS method for each vertical bin. The means and standard deviations for the three model simulations are shown as lines and shading: BASE (green), 3×Br (blue), and FastK (orange).
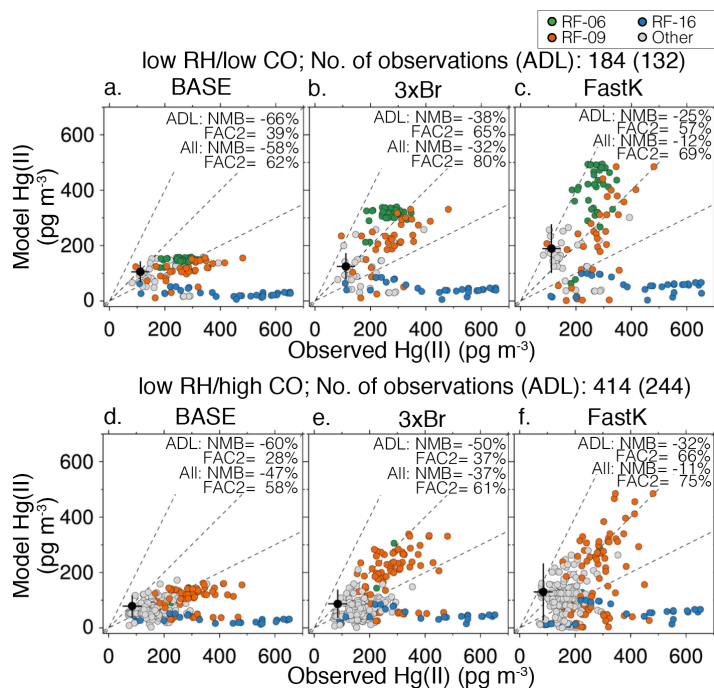
**Figure 5.** Scatterplot of observed and simulated concentrations of Hg(II) for the three model simulations in the **(a–c)** "low RH/low CO", and **(d–f)** "low RH/high CO" categories. Each column corresponds to our three GEOS-Chem simulations: BASE (left column), 3×Br (middle column) and FastK (right column). Observations for RF-06 (green), RF-09 (orange), and RF-16 (blue) are highlighted in color, with the remaining observations indicated by grey symbols. The black circles and error bars represent the mean and standard deviations of values below the detection limit (BDL) estimated with the ROS method for each air mass category separately and the corresponding simulated concentrations. The Normalized Mean Bias (NMB) and fraction of points where the model is within a factor of 2 of the observations (FAC2) are indicated on each panel (see text for definitions).
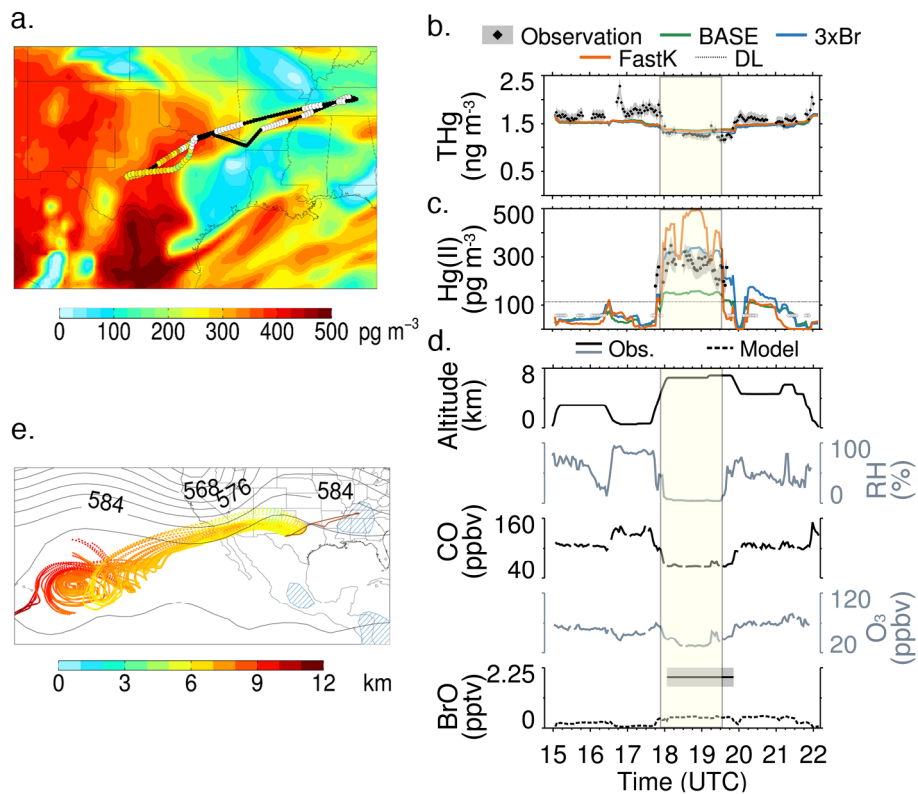
**Figure 6.** Case study for RF-06 on 19 June 2013. **(a)**, the C-130 flight track with circles color-coded based on observed Hg(II) concentrations (locations along the flight track with no Hg(II) observations are filled in black, and below the detection limit (BDL) observations are filled in white). The background map displays the GEOS-Chem Hg(II) concentrations at $450\,\mathrm{hPa}$ for $3\times\mathrm{Br}$ simulation between $17{:}00\text{--}20{:}00\,\mathrm{UTC}$. The timeseries of the observations of THg and Hg(II) are shown in **(b, c)**. The THg and Hg(II) measurements are represented by filled diamonds with the uncertainty represented by the gray shading. The dashed line represents the DL, and BDL observations are plotted at DL/2 with open circles. Modeled concentrations of THg and Hg(II) are displayed for the BASE (green line), $3\times\mathrm{Br}$ (blue), FastK (orange) simulations. Flight times where high Hg(II) concentrations were observed are highlighted. The timeseries of flight altitude, RH, CO, $O_3$ and BrO (observations and model) are shown in **(d)**. Panel **(e)** shows the $7\,\mathrm{day}$ HYSPLIT back trajectories for the highlighted sections of the flight. The contours show the NCEP/NCAR Reanalysis $500\,\mathrm{hPa}$ geopotential heights on 18Z for the day of the flight. The hatched areas show regions with greater than an average of $10\,\mathrm{mm\,day}^{-1}$ of surface precipitation for seven days before the flight.
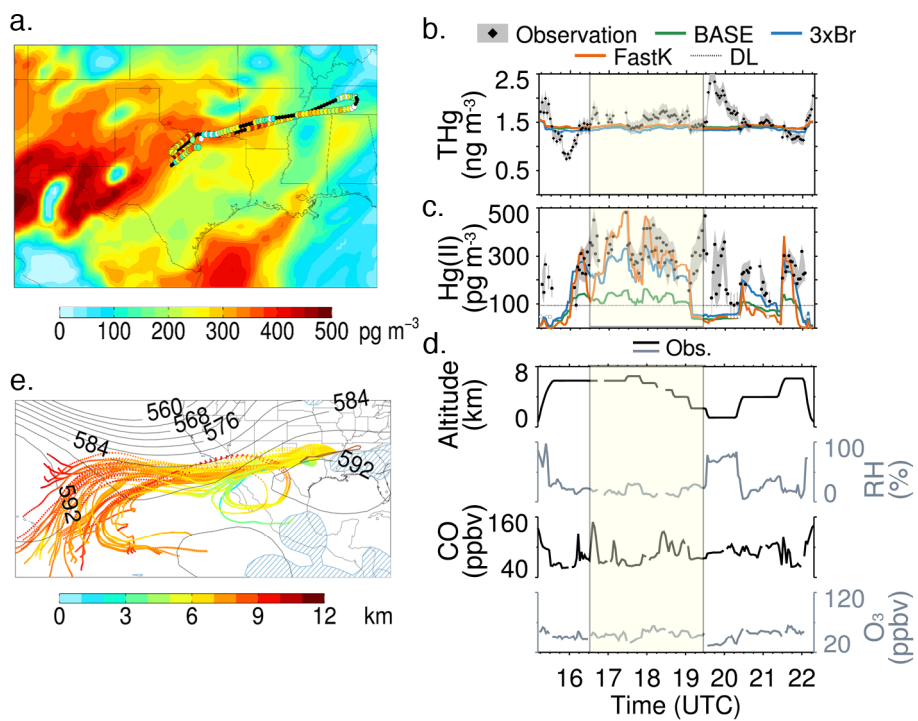
**Figure 7.** Case study for RF-09 on 24 June 2013. Same as Fig. 6, except that we do not show BrO concentrations which were not measured on this flight.
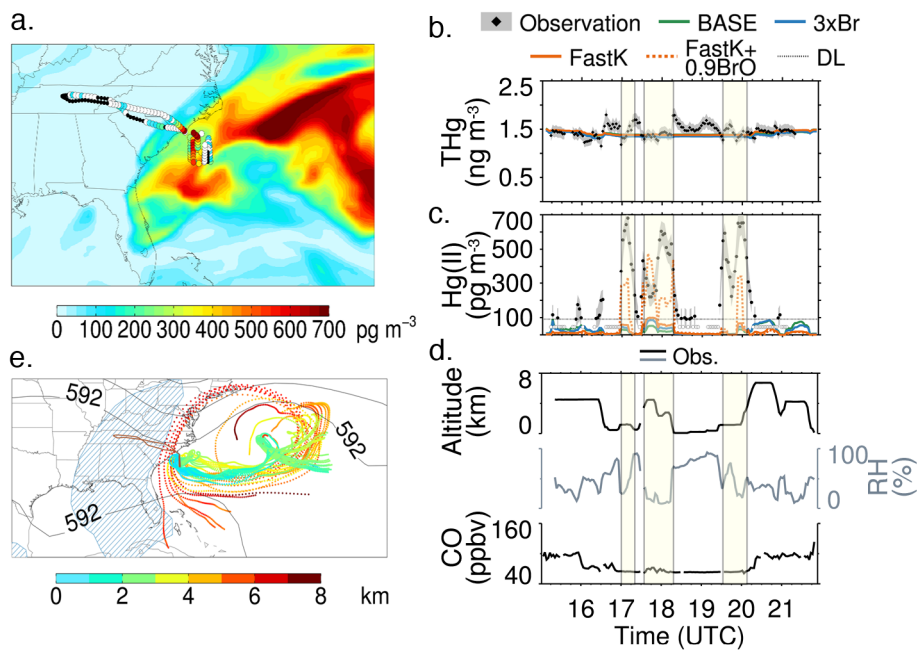
**Figure 8.** Case study for RF-16 on 8 July 2013. Same as Fig. 6, except the background map **(a)** displays Hg(II) concentrations at $800\,\mathrm{hPa}$ for the FastK $+ 0.9\mathrm{BrO}$ pptv simulation. Also we add the FastK $+ 0.9\,\mathrm{ppt}$ simulation as an orange dashed line in panels **(b, c)**. $O_3$ concentrations were not available for this flight and BrO concentrations were below the instrument's detection limit.
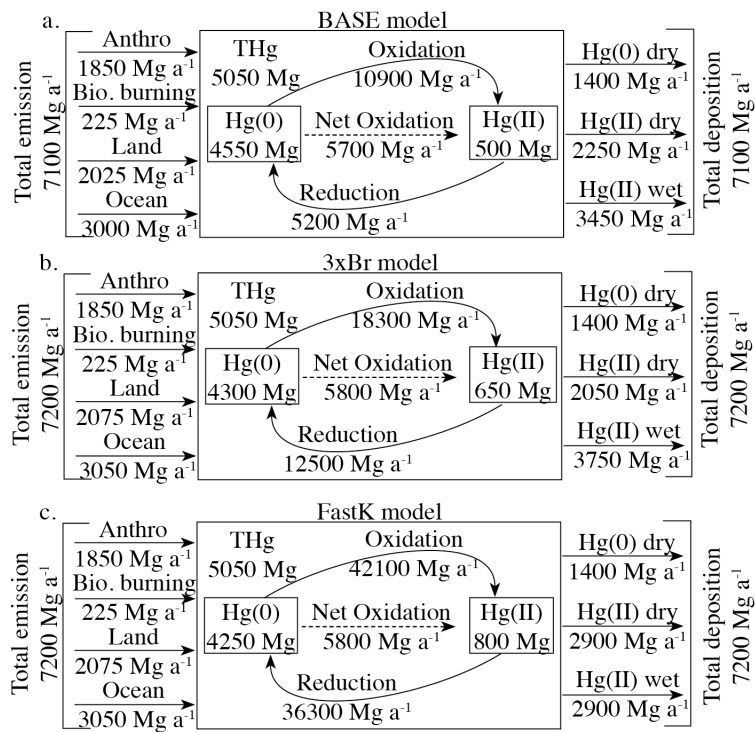
**Figure 9.** Annual global tropospheric budget of mercury in the **(a)** BASE, **(b)** 3×Br, and **(c)** FastK simulations for 2013. The burdens are in units of Mg ($10^6$ g) and the fluxes are in units of $\mathrm{Mg\,a^{-1}}$ (Mg per year).
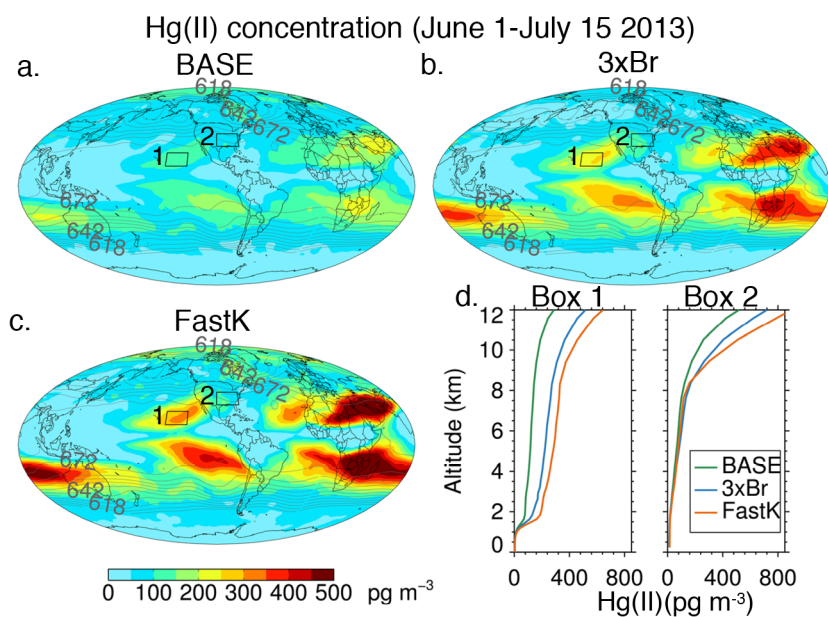
**Figure 10.** Average concentration of Hg(II) at 450 hPa during NOMADSS (1 June to 15 July 2013) for the **(a)** BASE, **(b)** 3×Br, and **(c)** FastK simulations. The contours show the NCEP/NCAR Reanalysis 450 hPa geopotential height averaged over the same period (contour interval: 6 decameter). Panel **(d)** indicates the mean modeled vertical profiles of Hg(II) concentrations for regions marked as "Box 1" and "Box 2" for the three simulations (BASE: green, 3×Br: blue, FastK: orange).
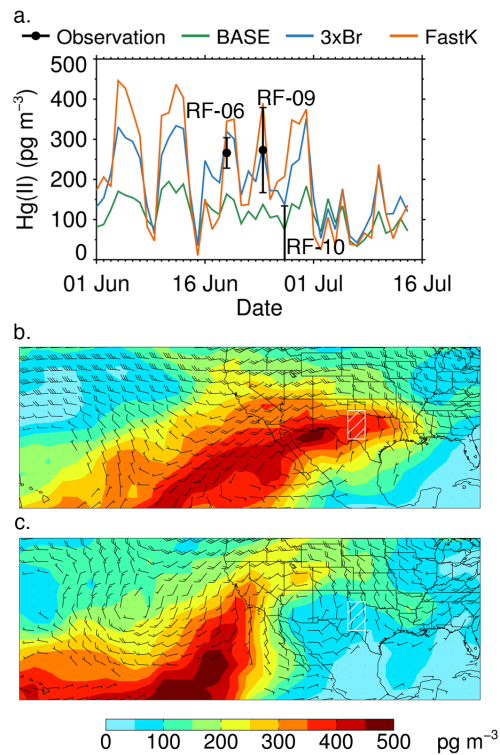
**Figure 11. (a)** Modeled timeseries of midday (noon-3 p.m.) Hg(II) concentrations at 6.5 km altitude over Texas (white rectangle shown in panels **(b, c)** for the three GEOS-Chem simulations (BASE: green, 3×Br: blue, FastK: orange) for 1 June–15 July 2013 and the mean and standard deviations of Hg(II) observations at 6–7 km over Texas for RF-06, RF-09 and RF-10. **(b)** mean midday FastK Hg(II) concentrations and winds at 6.5 km altitude for the 10 highest FastK Hg(II) concentrations from the timeseries in panel **(a)**. **(c)** Mean midday FastK Hg(II) concentrations for the 10 days with the lowest Hg(II) concentrations.